Nano Research

Open Access

Review Article

# Advances in metal halide perovskite ultrathin nanowires

Yejing Liu, Zhenyang Liu, Zhenhua Zhou, and Ou Chen ✉

*Department of Chemistry, Brown University, Providence, RI 02912, USA*

Cite this article: *Nano Research*, **2025**, *18*, 94907183. https://doi.org/10.26599/NR.2025.94907183

**ABSTRACT:** One-dimensional metal halide perovskite (MHP) nanowires (NWs) have recently emerged as highly promising optoelectronic materials due to their high aspect ratio, anisotropic quantum confinement, nonlinear optical response, unique mechanical flexibility, in addition to the well-known advantageous properties inherent to MHPs. In this review, we discuss the recent advancements in the synthesis, characterization, and properties of MHP NWs, particularly with their diameters below the Bohr radius (referred as ultrathin MHP NWs). Key future directions are highlighted, including refining synthesis methods for atomic-level control, understanding the growth mechanisms, improving stability through surface passivation, exploring lead-free alternatives to mitigate toxicity concerns, and achieving novel and unique properties. These advancements will enable ultrathin MHP NWs to play a pivotal role in advanced applications in various optical, optoelectronic, and photonic technologies.

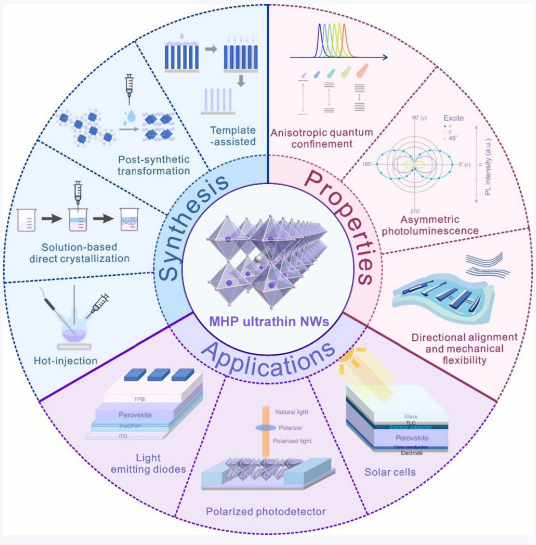


**KEYWORDS:** metal halide perovskites, ultrathin nanowires, anisotropic quantum confinement, synthesis, optical and optoelectronic properties

## 1 Introduction

Metal halide perovskite (MHP) nanocrystals (NCs) with a general formula of $ABX_3$ (A: monovalent cation; B: divalent metal cation; X: halide anion) have gained significant interest in recent years due to their unique crystal structure, ionic bonding nature, high defect tolerance, and exceptional optoelectronic properties [1–4]. These materials exhibit near-unity photoluminescence quantum yields (PLQYs), tunable bandgaps, and strong light absorption over a broad spectral range [5–8]. Moreover, their facile and low-cost synthesis, coupled with their high PL efficiency and sharp emission lines, make MHP NCs ideal candidates for various applications such as solar cells, light-emitting diodes (LEDs), lasers, photodetectors, and photocatalysts, [9–16] etc. The tunability of their optical properties by altering composition, and size, along with their capability to form diverse morphologies of nanostructures including zero-dimensional (0D) quantum dots (QDs), one-dimensional (1D) nanorods (NRs) and nanowires (NWs), and two-dimensional (2D) nanoplatelets (NPLs) and nanosheets, further import their versatility for implementation and integration into the above-mentioned applications [1, 17–24].

Among these different morphologies of MHP NCs, 1D NWs have garnered special attention due to their high aspect ratios and anisotropic quantum confinement, leading to distinct and unique electronic and optical properties [25–29]. In particular, when the thickness of these NWs is reduced below the Bohr diameter of the material, referred as ultrathin perovskite NWs or quantum wires (QWs), their optical and optoelectronic characteristics become highly tunable due to the presence of strong quantum confinement along their short radial dimensions [30–32]. In this case, the reduced dimensionality in ultrathin perovskite NWs enhances charge separation and transport along the long axial direction, while maintaining strong quantum confinement in the short radial direction [33–35]. This combination results in efficient anisotropic charge transport, which is advantageous for applications such as field-effect transistors, LEDs, and photodetectors [36–41]. Moreover, the high surface-to-volume ratio, high flexibility, and mechanical strength of ultrathin NWs makes them an excellent candidate for applications in sensors and catalysis, where largely exposed NW surfaces play a critical role [42–46].

**Received:** November 13, 2024; **Revised:** December 8, 2024
**Accepted:** December 11, 2024

✉Address correspondence to ouchen@brown.edu

While much progress has been made in the synthesis and modifications of 0D MHP NCs, controlling the diameter and uniformity of ultrathin NWs still remains a significant challenge. Traditional approaches, such as hot-injection and solvent-mediated reprecipitation methods, have been used to synthesize MHP NWs [30, 47, 48], but achieving uniform and controllable ultrathin diameters with high aspect ratios is still difficult. Furthermore, the stability of ultrathin perovskite NWs, especially under environmental stress (e.g., moisture, oxygen, and light exposure), remains a significant concern [48, 49], posing a major limitation for the practical implementation of such materials in real-world applications.

This review aims to provide a timely overview of the progress made in the synthesis, characterization, and applications of ultrathin perovskite NWs. Herein, we discuss the various methods applied to produce these structures, and highlight the critical challenges in achieving controlled nucleation and growth of ultrathin NWs with high morphological anisotropy. Additionally, we summarize the physical and chemical properties of ultrathin MHP NWs, with a focus on their optical behavior, structural stability, and potential for integration into advanced devices. Finally, we outline some key areas for future research, emphasizing the need for improved stability and tunability of these promising materials to fully realize their potential in optical, optoelectronic, photonic and many other applications.

## 2 Synthesis of ultrathin MHP NWs

### 2.1 Hot-injection method

In 2015, Protesescu et al. reported a reliable colloidal synthesis approach to firstly synthesize colloidal MHP particles in nanoscale with tunable sizes [31]. The synthetic approach is based on an injection process of preprepared A-site monovalent cation-carboxylic acid complex (such as Cs-oleate) into a mixture of B-site metal salt and organic ligands. MHP NCs start to grow instantly after the injection occurs at elevated temperature and stop growing by rapid temperature cooling using an ice-water bath. In 2016, Manna group modified the synthesis by replacing oleic acid with octanoic acid or hexanoic acid with shorter carbon chains, and decreasing the reaction temperature to below 70 °C [47]. They successfully prepared ultrathin $CsPbBr_3$ NWs with tunable thickness (NW diameter of 2.8, 3.4, 4.1, and 5.1 nm) by varying the concentration of the involved short acid over that of alkyl amines as shown in Figs. 1(a)–1(c). However, both the absorption and PL spectra of these NWs exhibited a lower energy shoulder/tail at ~ 500 nm indicating partial NW aggregation (Fig. 1(b)), revealing the instable nature of the produced ultrathin NWs. Differently, Yang group applied a hot injection method with typical long chain ligands (i.e., 1-dodecylamine, oleylamine, oleic acid) and a high reaction temperature (160 °C) to synthesize ultrathin $CsPbBr_3$ NWs along with other side products [30]. They further applied stepwise purifications to improve the NW purity, where ethyl acetate (EA) was used as the anti-solvent (Figs. 1(d)–1(f)). In each round of purification, the supernatant solution was collected and the precipitate was discarded after centrifugation. After three rounds of purifications, they obtained a relatively pure ultrathin $CsPbBr_3$ NWs (> 70% purity). However, the resulting ultrathin $CsPbBr_3$ NWs possessed a large amount of surface defects and thus a low emission efficiency due to significant ligand loss caused by the repeated purification processes using anti-solvent [7, 30].

### 2.2 Solution-based direct crystallization method

The ease of fabrication and processing at low temperatures is one of the most attractive features of MHPs, which not only reduces the fabrication costs and simplifies manufacturing processes, but also opens up new possibilities for large-area, flexible electronics [50–52]. The ligand-assisted reprecipitation (LARP) approach, typically carried out at room temperature (RT), has therefore attracted significant attention [53–55]. In this method, A- and B-

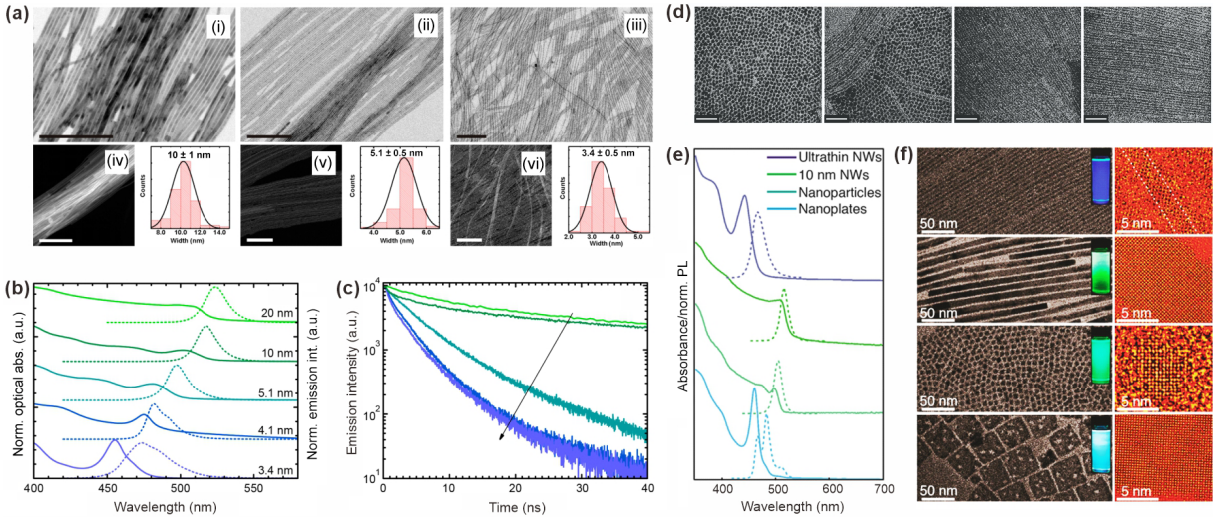


**Figure 1** (a) Representative bright field transmission electron microscopy (BF-TEM) and high-angle angular dark field scanning TEM (HAADF-STEM) images of $CsPbBr_3$ NWs with varying thicknesses: (i) and (iv) 10 nm, (ii) and (v) 5.1 nm, and (iii) and (vi) 3.4 nm. Scale bars represent 200 nm. Corresponding size distributions are shown. Short chain carboxylic acid to alkyl amine ratios are (i) and (iv) 0, (ii) and (v) 0.1, and (iii) and (vi) 0.3, respectively. (b) Optical absorption (solid line) and PL spectra (dashed line) for $CsPbBr_3$ NWs with different thicknesses. (c) Time-resolved PL decay profiles of $CsPbBr_3$ NWs excited at 405 nm, with an arrow indicating a thickness decrease from 20 to 3.4 nm. Reproduced with permission from Ref. [47], © American Chemical Society 2016. (d) TEM images illustrating stepwise purifications to obtain ultrathin $CsPbBr_3$ NWs, with scale bars of 50 nm. The ratio of EA to supernatant increases progressively from left to right. (e) Optical absorption (solid line) and PL spectra (dashed line) of $CsPbBr_3$ samples, ultrathin NWs, 10 nm thick NWs, nanoparticles and NPLs. (f) Corresponding transmission electron microscopy (TEM) and aberration-corrected high-resolution TEM (AC-HRTEM) images. Reproduced with permission from Ref. [30], © American Chemical Society 2016.

site cation salts are firstly dissolved in a good solvent, such as N,N-dimethylformamide (DMF) or dimethylsulfoxide (DMSO), along with ligands (e.g., oleylamine, oleic acid). Then, the resulting precursor solution is mixed with a poor solvent, such as toluene or hexane, to decrease the precursor solubility and trigger MHP crystallization to form NCs. In 2017, Amgar et al. employed this LARP technique to obtain ultrathin $CsPbX_3$ (X = Cl, Br, I) NWs [56]. The reaction was performed by adding hot Cs-oleate solution to a vial filled with oleic acid and oleylamine serving as organic ligands, followed by the addition of a $PbBr_2$ precursor solution in DMF. After 10 s of reaction, acetone was swiftly added as the anti-solvent to trigger NW crystallization. In addition, different amounts of hydrohalic acids (HX, X = Cl, Br, I) from 0–10 μL were introduced into the reaction system to tune the optical features through halide exchange reactions (Fig. 2(a)) [56]. The authors found that the length of obtained NWs was significantly shortened by increasing the added amount of HX acid, which was attributed to that the positively charged oleylammonia (i.e., protonated oleylamine) can perform similarly as $Cs^+$ cations to block the growth of MHP into long NWs [57, 58]. Unfortunately, the halide composition of obtained $CsPbX_3$ NWs was not homogeneous as reflected by the multiple emission peaks emerged in their PL spectra, indicating incomplete halide exchange. Around the same time, Kostopoulou et al. also applied the LARP method to synthesize $CsPbBr_3$ NWs and used anhydrous toluene to quench the reaction, resulting in a mixture of nonuniform NWs and NPLs [59]. The reaction solution was then kept under ambient conditions for one day without stirring. The NPLs were precipitated out of the solution while ultrathin $CsPbBr_3$ NWs were gradually formed in the supernatant. After one week, however, the NW thickness progressively increased from 2.6 to 6.1 nm with a broader thickness distribution [59]. In 2019, while utilizing the LARP method to synthesize ultrathin NWs, Peng group added acetonitrile (ACN) into toluene with different proportions to act together as the antisolvent [60]. The synthesized MHP NCs exhibited a morphological transition from nanocubes (with no added ACN) to NWs (with toluene/ACN = 90:10) and further to NW bundles (with toluene/ACN = 80:20) (Fig. 2(b)). Further increasing the ACN amount led to broader and weaker absorption peaks together with the formation of large perovskite crystals that precipitated out of the reaction solution [60]. The authors attributed the results to the addition of the polar solvent ACN, which promoted oleylamine protonation and acted as a Lewis base, forming dative N→Pb bonds on the NW surfaces, thereby restricting isotropic growth of $CsPbBr_3$ (Fig. 2(c)) [61]. However, they did not conduct further research to identify the specific facets where growth was inhibited. In 2022, Hu et al. applied a modified LARP method to synthesize ultrathin $CsPbI_3$ perovskite NWs (Figs. 2(d)–2(g)) [62]. Instead of traditional polar solvents (DMF, DMSO), they used a low-polar organic medium (toluene) to dissolve precursor-ligand complexes (Cs-oleate, $PbI_2$-oleylamine). Different from the red emission (peaked at ~ 700 nm) from $CsPbI_3$ NCs, they obtained ultrathin $CsPbI_3$ NWs with single-halide component, which presented a blue-shifted emission peaked at 599 nm. A further blue-shifted yellow emission (at 558 nm) with a record high PLQY of 94% was obtained by adding $ZnI_2$ precursor into the reaction system [62].

In addition, Huang and his co-workers reported another room-temperature colloidal synthesis of ultrathin $CsPbBr_3$ NWs in 2017 [63]. In their reaction system, the precursor solutions were stirred continuously under RT, followed by direct centrifugation. They further applied a post-synthetic heat treatment process (at 120 °C for 2 min) to the as-synthesized NWs, which enhanced the PLQY

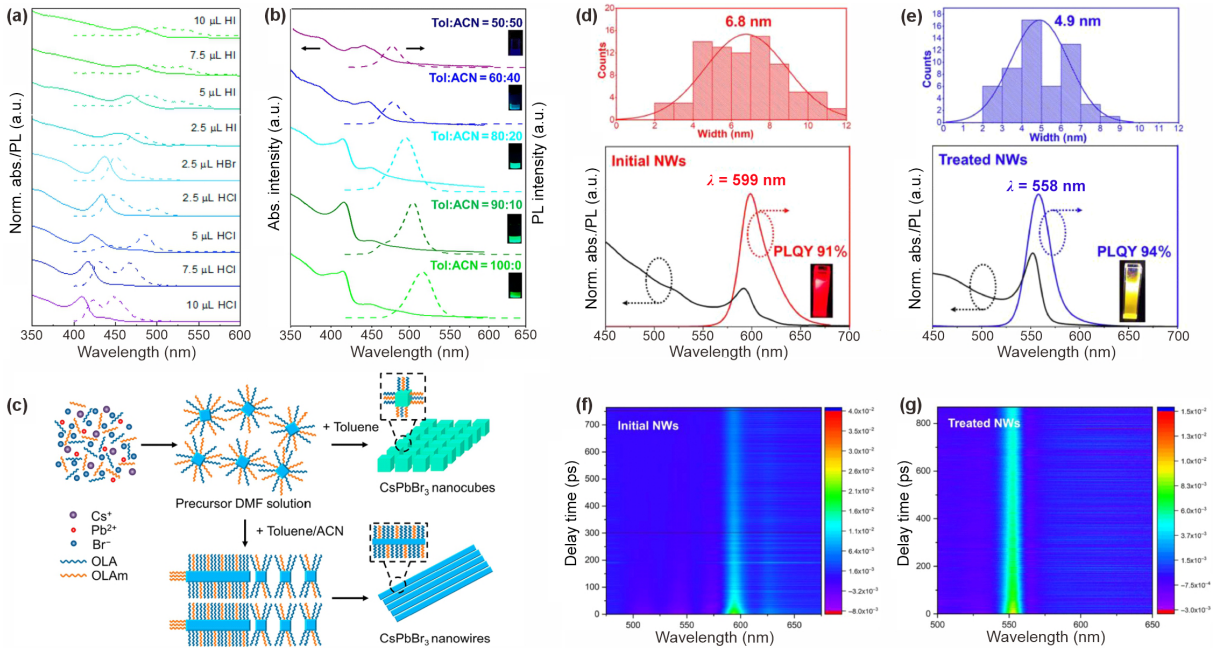


**Figure 2** (a) Optical absorption (solid line) and PL spectra (dashed line) of $CsPbX_3$ NWs synthesized with varying amounts of HI, HBr, and HCl. Reproduced with permission from Ref. [56], © American Chemical Society 2017. (b) Optical absorption (solid line) and PL spectra (dashed line) of $CsPbBr_3$ NCs synthesized at different volume ratios of toluene/ACN. (c) Schematic diagram illustrating the formation processes of $CsPbBr_3$ nanocubes in toluene and ultrathin NWs in toluene/ACN. Reproduced with permission from Ref. [60], © American Chemical Society 2019. (d) Thickness distribution (top) and corresponding absorption and PL spectra (bottom) of ultrathin $CsPbI_3$ NWs. (e) Thickness distribution (top) and corresponding absorption and PL spectra (bottom) of $ZnI_2$-treated ultrathin $CsPbI_3$ NWs. Pseudo-color femtosecond transient absorption (TA) measurements for the ultrathin $CsPbI_3$ NWs before (f) and after (g) $ZnI_2$ treatment. Reproduced with permission from Ref. [62], © Elsevier Ltd. 2022.

of the NWs from less than 1% to over 20% [63]. This process was accompanied by red-shifted absorption and PL peaks, indicating an increase of NW thickness.

### 2.3 Post-synthetic transformations

Post-synthetic chemical and/or particle shape transformations have been widely employed in MHP NCs to enhance their compositional and morphological tunability [5, 64–66]. This versatile approach enables precise modifications of pre-synthesized NCs, offering access to a broader range of colloidal nanostructures that may be challenging or even impossible to achieve through direct synthesis [67, 68]. Taking advantage of this post-synthetic transformation approach, researchers can fine-tune the properties of NCs, such as their optical and electronic behavior, and gain valuable insights into the mechanisms underlying their growth [69–72].

In 2018, Li et al. applied a thiourea-assisted post-synthetic treatment to convert $CsPbBr_3$ nanocubes into ultrathin $CsPbBr_3$ NWs [73]. A thiourea aqueous solution was directly introduced into the crude organic solution of $CsPbBr_3$ nanocubes to extract $Pb^{2+}$ cations by forming stable $Pb^{2+}$-thiourea complexes. Under mild heating at 35 °C, the $CsPbBr_3$ nanocubes firstly transformed into $Cs_4PbBr_6$ NCs with a zero-dimensional perovskite structure (Fig. 3(a)). And CsBr was subsequently removed by water due to its high water solubility, further transforming $Cs_4PbBr_6$ into small $CsPbBr_3$ NCs, which evolve into ultrathin $CsPbBr_3$ NWs [73]. The resulting NWs showed good colloidal stability and a high PLQY of 60%, albeit with a PL shoulder peak at around 500 nm attributed to nanocube impurities. The high PLQY was explained by the $PbBr_2$ rich surface of the obtained ultrathin $CsPbBr_3$ NWs evidenced by X-ray photoelectron spectroscopy (XPS) measurements [73, 74].

In 2021, Chen group reported a synthesis of ultrathin $CsPbBr_3$ NWs via a post-synthetic transformation process starting from 0D $Cs_4PbBr_6$ perovskite NCs, using short alkyl chain organic ligands (Figs. 3(b) and 3(c)) [75]. In the transformation reaction, $PbBr_2$ precursor together with different organic ligands (i.e., oleic acid, hexanoic acid and octylamine) were added under mild heating condition at 50 °C. After two hours, ultrathin $CsPbBr_3$ NWs were produced with high purity. Mechanism studies showed that the $PbBr_2$-ligand intermediates, which exhibited lamellar structures, served as anisotropic templates directing the growth of $CsPbBr_3$ NWs [75]. Consistent with the proposed NW growth mechanism, the authors showed that the $PbBr_2$-ligand intermediates with larger *d*-spacings tended to produce $CsPbBr_3$ nanocubes, while intermediates with smaller *d*-spacings favored the formation of ultrathin NWs [75].

Besides synthesizing ultrathin $CsPbBr_3$ NWs through post-synthetic transformation processes, post-synthetic halide exchange reactions were commonly used to produce ultrathin $CsPbX_3$ NWs containing $Cl^-$ or $I^-$ ions by introducing HX or $MX_2$ (M = Pb or Zn, X = Cl or I) precursors to the pre-synthesized $CsPbBr_3$ NWs solution [30, 56, 60]. In these cases, continuous blue-shifted and red-shifted emission peaks can be observed in Br-to-Cl and Br-to-I anion-exchange reactions, respectively (Fig. 3(d)), demonstrating higher emission tunability by successful inclusion of Cl- and I-component to the ultrathin $CsPbX_3$ NWs.

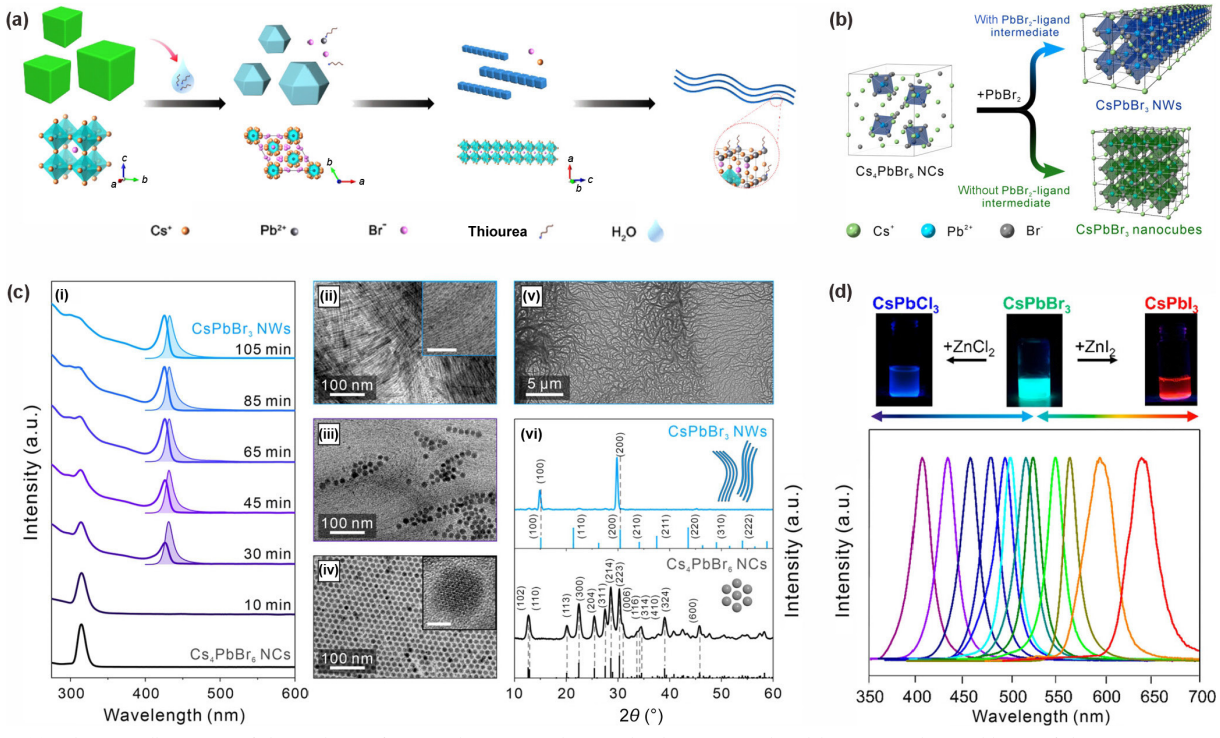


**Figure 3** (a) Schematic illustration of the evolution from $CsPbBr_3$ nanocubes to ultrathin NWs induced by post-synthetic addition of thiourea aqueous solution. Reproduced with permission from Ref. [73], © American Chemical Society 2018. (b) Schematic diagram illustrating the conversion from 0D $Cs_4PbBr_6$ perovskite NCs to either ultrathin $CsPbBr_3$ NWs or $CsPbBr_3$ nanocubes through selective reaction pathways. (c) Evolution of structure, morphology, and optical properties during the reaction illustrated by: (i) optical absorption and PL spectra depicting the transition from $Cs_4PbBr_6$ NCs to ultrathin $CsPbBr_3$ NWs over time; Corresponding TEM images showing the evolution from (iv) $Cs_4PbBr_6$ NCs to (iii) a mixture of $Cs_4PbBr_6$ NCs and newly formed $CsPbBr_3$ NWs, and then (ii) ultrathin $CsPbBr_3$ NWs; (v) Low-magnification TEM image of NW bundles; (vi) X-ray diffraction (XRD) patterns of starting material and final product. Reproduced with permission from Ref. [75], © American Chemical Society 2021. (d) Photographs of ultrathin $CsPbX_3$ (X = Cl, Br, I) NW solutions produced via anion exchange (top) and their respective normalized PL spectra (bottom). Reproduced with permission from Ref. [60], © American Chemical Society 2019.

### 2.4 Template-assisted method

Template-based space-confined growth method has garnered significant attention as an effective strategy for fabricating NWs with high crystallinity and precisely controlled thickness [76–78]. By utilizing templates with desired nanoscale channels, researchers can precisely control the NC growth process, leading to uniform and high-quality nanostructures [79–81]. This method enables the formation of NWs with precisely defined dimensions, resulting in ligand-free MHP NWs that typically exhibit superior structural and property stabilities compared to colloidally synthesized MHP NWs [82, 83].

In 2016, the Kovalenko group utilized mesoporous silica (meso-$SiO_2$) matrices as templates to synthesize elongated perovskite NCs with sizes falling within the strongly quantum-confined regime [84]. High-concentration CsX and $PbX_2$ precursor salt solutions were infiltrated into the pores of meso-$SiO_2$ templates, which featured hexagonally ordered 1D channels with varying pore diameters (2.5–7 nm), followed by vacuum drying. The resulting ultrathin, elongated MHP NCs, confined within the meso-$SiO_2$ matrix, exhibited an ordered mesoporous structure composed of 1D channels resembling NW structures. The bright emissions of these template-synthesized NCs could be finely tuned by pore-size-dependent quantum size effects as well as chemical compositions [84]. In 2019, Zhang et al. developed a self-assembled templating process to fabricate ultrathin $CsPbBr_3$ NWs [85]. Confined nanochannels were formed by well aligned polymethyl methacrylate (PMMA) fibers through an electrospinning process as shown in Fig. 4(a). These nanochannels acted as templates for the formation of NWs from the infiltrated precursor solutions [85]. After the solvent (DMF) evaporated, ultrathin $CsPbBr_3$ NWs with a diameter of ~ 2 nm were obtained within the electrospun PMMA fibers. In addition, $CsPbBr_3$ nanobelts and nanocubes can also be produced by extending the stirring time of the initial DMF precursor solution (Figs. 4(b)–4(e)). In 2022, Fan group used nanoporous anodic aluminum oxide (AAO) as templates to fabricate ultrathin $CsPbBr_3$ NWs [86]. AAO templates with an initial pore diameter size of around 6.6 nm, were fabricated through an anodic anodization process at a low voltage. Subsequent $Al_2O_3$ coating via atomic layer deposition (ALD) reduced the pore size from ~ 6 to 2.8 nm (Fig. 4(f)) [86]. Using this AAO template, ultrathin $CsPbBr_3$ NWs were fabricated by filling the nanopores through a low-pressure closed space sublimation process. More recently, Yang group in 2023 developed a system that utilized single-walled carbon nanotubes (with a diameter of 1.2–1.4 nm) as templates to produce single-unit-cell thick Cs-Pb-I NWs, which can be suspended on monolayer graphene TEM grids [87]. Due to the stability of graphene and carbon nanotubes against heat and polar solvents, they were able to remove the perovskite crystals formed outside the templates using polar solvents and prevent carbon contaminations by annealing at high temperatures [87]. This approach enabled direct *in situ* observation of atomic activities inside the MHP framework, which had only been accessible through theoretical calculations prior to the work [88, 89].

### 2.5 Solvothermal method

Solvothermal method has also been employed for the synthesis of perovskite NWs with high crystallinity and morphological uniformity [90–93]. This technique involves dissolving precursor materials in a solvent at elevated temperatures and pressures, creating an environment conducive to controlled crystal growth [94–96]. In 2017, Chen et al. applied this method to successfully obtain ultrathin $CsPbBr_3$ NWs with a morphological purity [91]. Specifically, the synthesis of ultrathin NWs was realized by pre-dissolving the Cs and Pb precursors with ligands (i.e., oleic acid and oleylamine) inside a glovebox and then transferred into the autoclave. The reaction was carried out at 160 °C and the resultant $CsPbBr_3$ NWs exhibited a thin diameter of 2.6 nm with an absorption peak at 445 nm [91].

## 3 Current understanding of formation mechanisms for ultrathin MHP NWs

MHP NCs possess highly ionic nature with relatively low formation energies, which leads to rapid nucleation and growth kinetics typically within a timescale of sub-second to a few seconds [97, 98]. This makes *in situ* monitoring of the nucleation and growth events

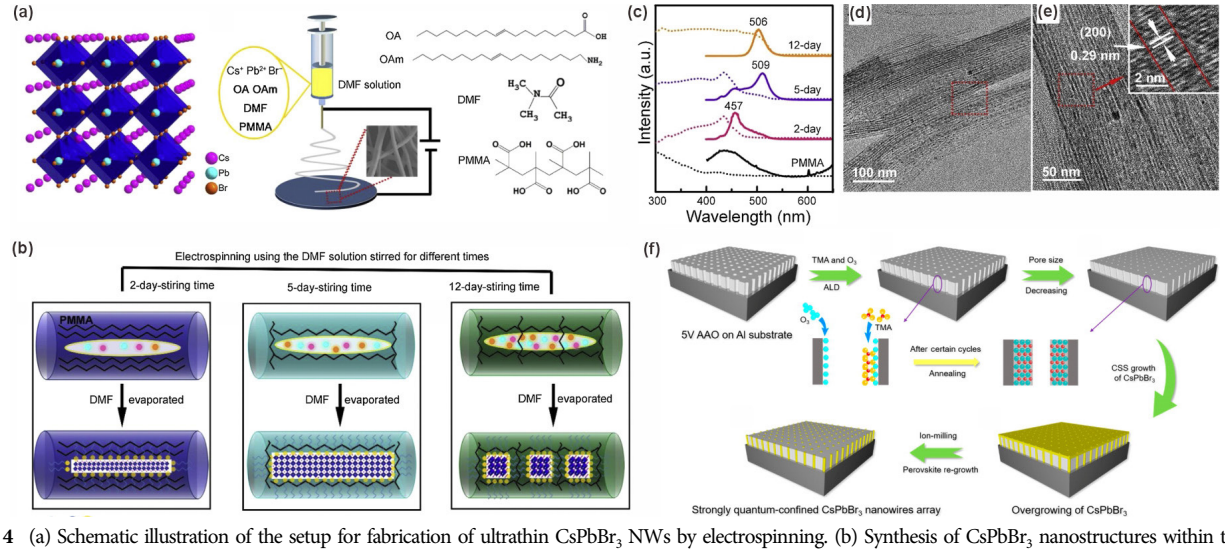


**Figure 4** (a) Schematic illustration of the setup for fabrication of ultrathin $CsPbBr_3$ NWs by electrospinning. (b) Synthesis of $CsPbBr_3$ nanostructures within the self-assembled nanoscale templates of electrospun PMMA fibers using the DMF solutions stirred for different times. (c) Optical absorption (dashed line) and PL spectra (solid line) of $CsPbBr_3$ products prepared. (d) and (e) TEM images of ultrathin $CsPbBr_3$ NWs after removing PMMA. Reproduced with permission from Ref. [85], © Elsevier Ltd. 2019. (f) Schematic process flow of the AAO template-assisted synthesis of ultrathin $CsPbBr_3$ NWs array. Reproduced with permission from Ref. [86], © American Chemical Society 2022.

to understand the formation mechanism of ultrathin MHP NWs quite challenging [97, 99]. Despite this challenge, researchers have made some important progresses in uncovering key factors that influence the synthesis of ultrathin MHP NWs to help understand their formation mechanisms.

### 3.1 Seed-mediated growth

Chen et al. discovered that pre-dissolving the precursors was crucial for successful preparations of MHP NWs, otherwise, MHP nanocubes would form instead [91]. They employed a seed-mediated growth mechanism to explain this phenomenon (Fig. 5(a)). When the Cs and Pb precursors are directly heated without pre-dissolution, the gradual dissolving process limits the concentration of effective monomers in solution at any given reaction stage. Consequently, a relatively low number of small nuclei seeds formed in solution, which then grow into nanocubes, a morphology driven by thermodynamic stability with a limited monomer supply rate during the course of the particle formation reaction [91]. In contrast, when the precursors are pre-dissolved, a high concentration of active monomer ions becomes instantly available upon mixing the Cs and Pb precursors, leading to the rapid formation of a large number of small nuclei seeds [91]. Under this condition, ultrathin NWs merge through a seed-mediated anisotropic growth process caused by assembly and orientate attachment of the initial seed nuclei, yielding MHP NWs with enlarged aspect ratios [91, 100].

### 3.2 Oriented attachment

Besides the ripening process described by the LaMer growth model [101], oriented attachment has emerged as another key mechanism for NW growth [102–104]. In this process, smaller NCs align and fuse along specific crystallographic orientations to form larger

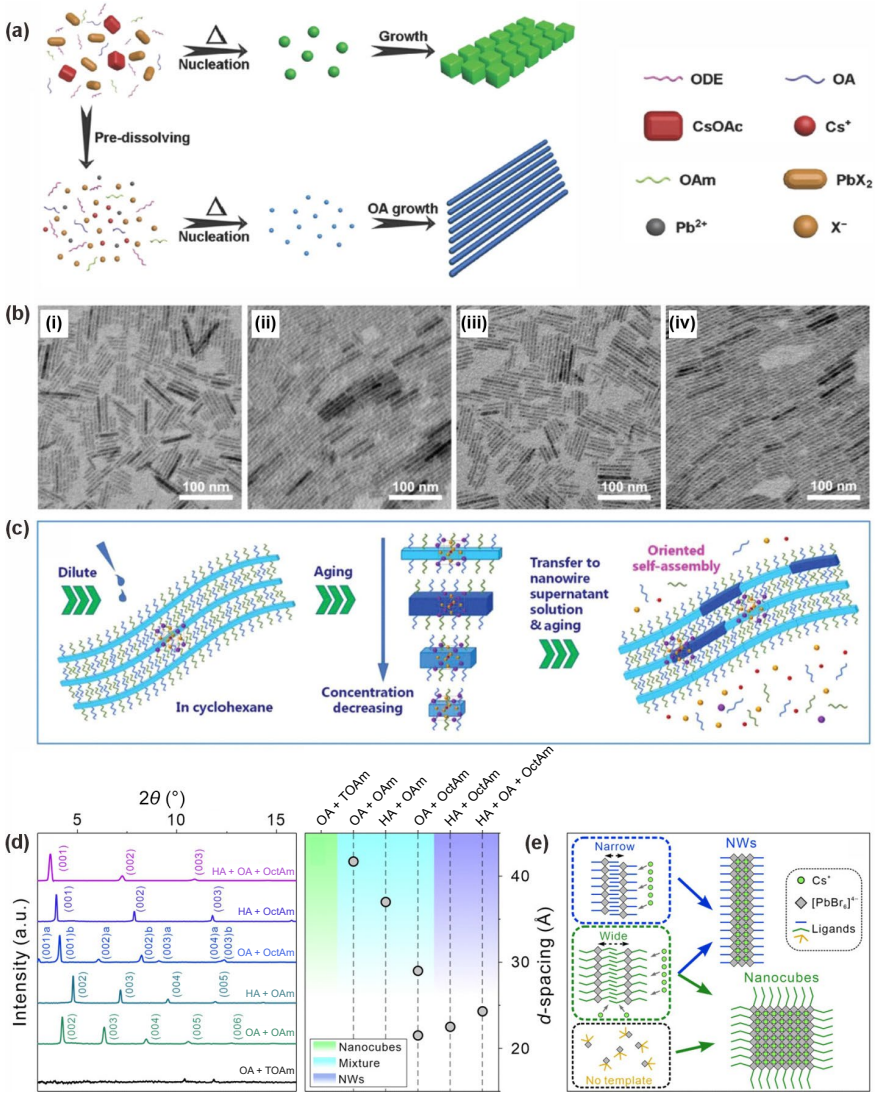


**Figure 5** (a) The proposed seed-mediated growth process of $CsPbBr_3$ nanocubes and ultrathin NWs formation without and with precursor predissolving. Reproduced with permission from Ref. [91], © WILEY-VCH Verlag GmbH & Co. KGaA, Weinheim 2017. (b) TEM/HRTEM images of $CsPbBr_3$ ultrathin NRs and NWs: (i) and (iii) the NRs formed by dispersing NWs in cyclohexane with increasing concentrations, (ii) and (iv) the NWs formed by aging from NRs. (c) Schematic illustration of the transformations between $CsPbBr_3$ NRs and NWs. Reproduced with permission from Ref. [49], © Wiley-VCH GmbH 2021.(d) Small-angle XRD patterns of the $PbBr_2$-ligand intermediates (left). The correlation between *d*-spacing of the $PbBr_2$-ligand intermediates and the morphology of the transformation product from $Cs_4PbBr_6$ NCs. (e) Schematic illustration of the template-based formation mechanism of $CsPbBr_3$ NWs or nanocubes. Reproduced with permission from Ref. [75], © American Chemical Society 2021.

nanostructures like NWs to minimize the exposure of high-energy crystal facets [105–107]. Previous reports have demonstrated the transformation of MHP materials from 0D NCs to 1D NWs over time [102]. Kostopoulou et al. observed short, bullet-like MHP NRs from the quenched aliquots in the LARP synthesis, sharing the same growth direction with the longer, ultrathin perovskite NWs finally produced [59]. They attributed the formation and thickening of ultrathin NWs to the oriented attachment mechanism [59]. Specifically, individual ultrathin NRs align and fuse together along anisotropic directions, e.g., [$\bar{1}$10] crystal direction, forming longer, single-crystalline ultrathin NWs [59]. Supporting this mechanism, Wang et al. examined the transformation between ultrathin NWs and NRs [49]. They found that ultrathin $CsPbBr_3$ NWs prepared in cyclohexane became unstable upon dilution, which would decompose and transform into NRs. The resulting NRs possessed higher aspect ratios when the initial NW concentration was higher [49]. They explained this wire-to-rod transformation by the desorption of ligands and extra precursor ions, which stabilized the NWs. This departure of stabilizing agents led to the breakdown of the NW structure post-dilution [49, 108]. The subsequent increases in the length and thickness of produced NRs over time can be explained by the Ostwald ripening mechanism [101]. Interestingly, when the collected precipitates of $CsPbBr_3$ NRs were redispersed in the supernatant solution, they transformed back into NWs after aging for four days. The resultant NW thickness matched the initial NR diameter (Fig. 5(b)). The authors showed that the NRs that were either too thick or too thin failed to connect with others, supporting their hypothesis that NW formation occurs through end-to-end self-assembly and oriented attachment of NRs (Fig. 5(c)) [49].

### 3.3 Ligand regulated formation

It is widely recognized that ligands are crucial in directing the morphology of perovskite NCs, as they strongly influence interactions among the precursors and intermediate structures during synthesis [109–112]. Given the limited solubility of $PbBr_2$ precursor in nonpolar solvents (e.g., hexane and toluene), Chen group hypothesized that the formation of ultrathin NWs can be regulated by ligands that govern the configuration of $PbBr_2$-ligand intermediates [75]. To explore this, they applied various ligand combinations to form different $PbBr_2$-ligand intermediates in toluene, each displaying a lamellar structure as evidenced by a set of {00*l*} diffraction peaks in their XRD patterns (Fig. 5(d)). They discovered that ligand combinations producing $PbBr_2$-ligand intermediates with smaller *d*-spacings promoted the exclusive formation of ultrathin $CsPbBr_3$ NWs [75]. They further proposed that these lamellar $PbBr_2$-ligand intermediates not only serve as a source of precursor, but also act as an anisotropic template guiding the NW growth. Supporting this hypothesis, they replaced the linear alkyl-amine ligands with a branched trioctylamine ligand, which did not form layered intermediate configurations, and only $CsPbBr_3$ nanocubes emerged as the sole final product (Fig. 5(e)) [75].

## 4 Characterizations, properties, and applications of ultrathin MHP NWs

### 4.1 Morphological and crystal structure determinations

Due to their small diameter, low image contrast, and instability under electron beam illumination, it could be quite challenging to directly image ultrathin MHP NWs using conventional TEM [113]. To overcome the challenge, Imran et al. in 2016 employed a direct-electron detection camera to replace the conventional charge-coupled device (CCD) camera in their high resolution (HR)-TEM measurements [47]. They found that the ultrathin $CsPbBr_3$ NWs they synthesized were confined along the [110] crystal direction and elongated along the [1$\bar{1}$0] direction (Fig. 6(a)). Differently, thicker $CsPbBr_3$ NWs (thickness of ~ 10 nm) grew along the [001] crystal axis while being constricted along the [110] crystal direction (Fig. 6(a)) [47, 114]. They explained this difference by the inhibited growth along the [001] direction after addition of short chain acids during NW synthesis [25, 114]. Besides TEM, the authors also applied atomic force microscopy (AFM) technique to visualize their ultrathin MHP NWs [47]. By tracing the cross-section profile, Imran et al. found that the ultrathin $CsPbBr_3$ NWs exhibited a rectangular cross-section, rather than a cylindrical one [47].

In the same year, Zhang et al. used aberration-corrected HR-TEM (AC-HR-TEM) to enhance the image resolution and minimize the beam damage by limiting the applied electron doses [30]. In this way, the spherical aberration, chromatic aberration and astigmatism caused by electric lens can be largely compensated [115, 116]. To prevent the beam damage and achieve atomic-resolution imaging of ultrathin perovskite NWs, Yang group recently applied single-walled carbon nanotubes to confine individual Cs-Pb-I NWs with even single-unit-cell thickness [87]. Since both the graphene substrate and carbon nanotubes can provide NWs from heating, irradiation, and moisture, they were able to use conventional TEM and scanning TEM (STEM) techniques to directly visualize the atomic structure of individual ultrathin NWs without degradation (Fig. 6(b)). Unlike bulkier $CsPbI_3$ crystals, which commonly exhibit an edge-shared non-perovskite δ-phase structure [117], the atomically thin NW confined in a nanotube displayed a stable corner-shared perovskite phase (Fig. 6(b)). The observed co-existence of α-phase and δ-phase in thicker NWs indicated that geometrical confinement could help stabilize the photoactive α-phase perovskite [87, 118]. However, the lead-iodide octahedral units of these NWs were largely distorted, composed of a contracted cesium framework and an expanded iodine framework (Fig. 6(c)) [87]. Interestingly, they found that the orientation of each octahedral units varied under each STEM scan (Fig. 6(c)), which could result from their intrinsic structure instability and/or NW rotation [119]. To gain further dynamical insights, they applied AC-HR-TEM along with a high-efficiency direct-electron detection camera with a wide range of electron dose rates to achieve atomic resolution and high frame rates, capturing transient structural dynamics *in situ* [87]. This setup allowed them to trace each atom column over time using atom-tracing algorithms, enabling them to reconstruct the dynamic behaviors of MHP NWs at unprecedented resolution.

To determine the crystallographic information of ultrathin MHP NWs, XRD patterns are typically measured and analyzed [49, 59]. These ultrathin MHP NWs exhibit non-uniform diffraction peak broadening due to their anisotropic 1D morphology [120, 121]. For example, in the case of $CsPbBr_3$ NWs with a cubic phase, the (100) diffraction peak is significantly narrower than other diffraction peaks due to the large crystallite size only along the wire axial [001] direction [63]. Moreover, the diffraction peaks of ultrathin MHP NWs often shift to smaller angles (i.e., larger *d*-spacings) compared to their standard patterns, signifying substantial lattice expansions

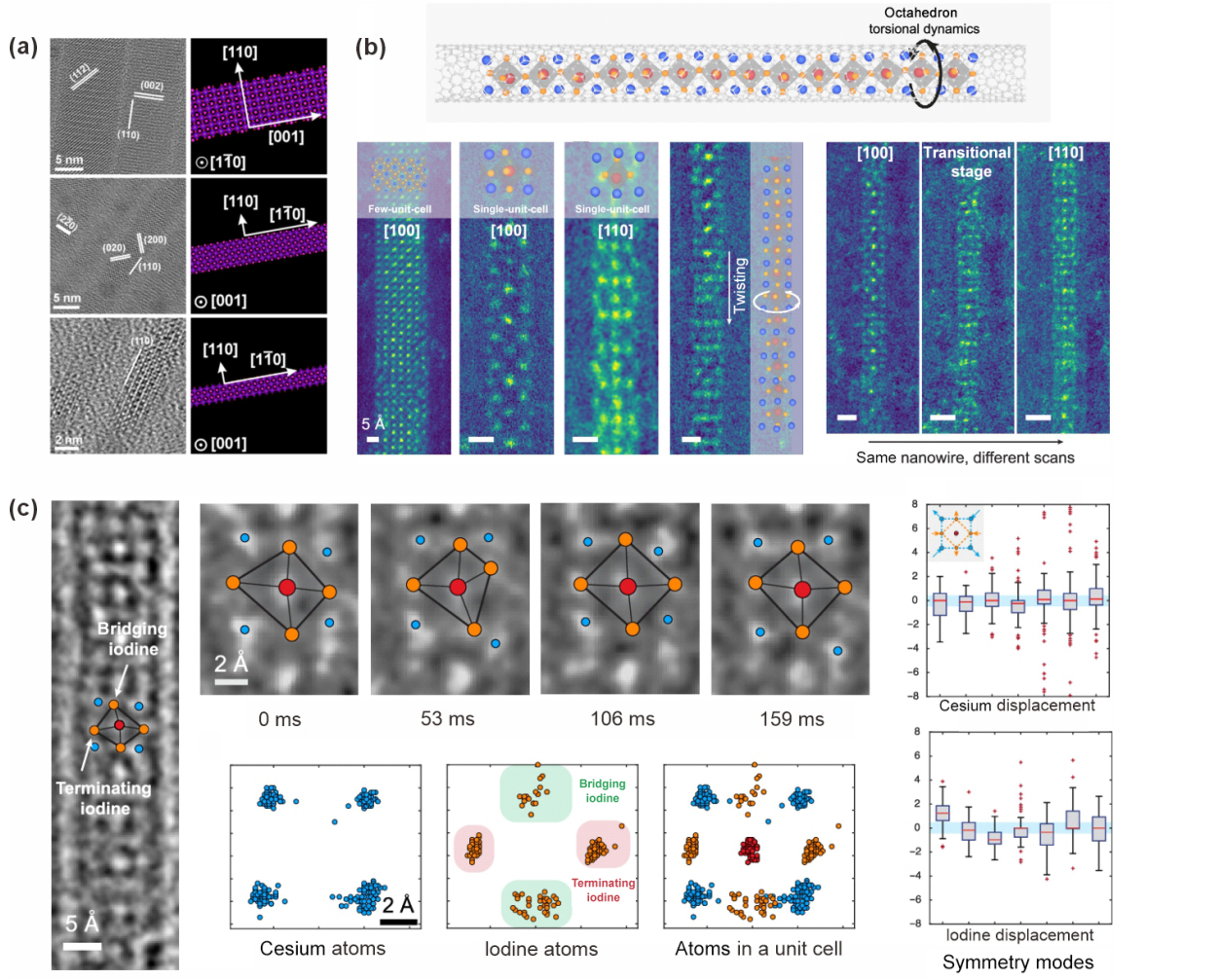


**Figure 6** (a) Wide field of view (FOV) HR-TEM images and schematic crystallographic models of synthesized $CsPbBr_3$ NWs with widths of 10 nm (top row), 5.1 nm (middle row) and 3.4 nm (bottom row). Reproduced with permission from Ref. [47], © American Chemical Society 2016. (b) Schematic model of 1D Cs-Pb-I NWs confined in single-walled carbon nanotubes (top). ADF-STEM characterization of the static structure of atomically thin 1D Cs-Pb-I NWs, viewed along [100], [110], [011] directions, and structural change of the same NW during different scans. (c) Transient structural distortion of individual Pb-I octahedral units, illustrated by atomic-resolution TEM images of Cs-Pb-I NW segments, real-time trajectories of cesium (blue), lead (red) and iodine (orange) atoms, and unit-cell framework distortion of cesium and iodine decomposed based on seven symmetry modes of a square. Reproduced with permission from Ref. [87], © American Chemical Society 2023.

[75]. This lattice expansion occurs because the high surface-to-volume ration in these NWs causes a large fraction of atoms to be located on the NW surface, causing surface relaxation to minimize total energy [122]. In addition, due to their strong inter-NW van der Waals interactions, ultrathin MHP NWs tend to bundle together upon solvent evaporation, potentially influencing XRD measurements by promoting specific orientations on the substrate [49, 120]. For instance, Yang et al. demonstrated that the $CsPbBr_3$ NWs showed exclusively a set of {*h*00} peaks in the measured XRD pattern, indicating a high degree of NW alignment on the substrate [75]. These factors may complicate the unambiguous determination of the crystal structure for ultrathin MHP NWs. Therefore, complementary techniques, such as TEM, are often necessary to accurately resolve the crystal phase of synthesized ultrathin MHP NWs [123]. Selected area electron diffraction (SAED) measurements can provide localized diffraction information, offering valuable support for phase identification, particularly in NW samples with particle shape irregularities [124, 125].

Small-angle X-ray scattering (SAXS) is another powerful technique for NW characterization, offering insights into their size, shape, orientation, and structural uniformity [126]. Zhang et al. analyzed SAXS patterns for ultrathin $CsPbBr_3$ NWs, revealing a prominent diffraction ring that reflected their periodic packing along the radial direction [30]. The calculated *d*-spacing (4.63 nm) corresponded to the NW diameter (~ 2.2 nm) with the addition of two layers of surfactants. Furthermore, the narrow width of the diffraction peak indicated excellent diameter uniformity in the synthesized ultrathin NWs [30].

### 4.2 Unique optical, electrical and optoelectronic properties of ultrathin MHP NWs towards applications

One unique property of ultrathin MHP NWs, compared to thicker NWs or NRs, is the presence of strong anisotropic quantum confinement effect, which is reflected by optical absorbance and PL spectra of these ultrathin NWs. As the NW diameter decreases, quantum confinement intensifies, enlarging the material's bandgap and resulting in significant blueshifts in both excitonic absorption and PL peaks [63, 85, 127]. For example, the reported ultrathin $CsPbBr_3$ NWs exhibited tunable first excitonic absorption peak position from 413 to 484 nm (Table 1), significantly bluer than the

typical absorption peak position of their nanocube or bulk crystal counterparts (> 500 nm) [4, 128]. This strong anisotropic quantum confinement effect may contribute to the high PLQYs of MHP NWs, despite their extensive exposed surfaces and lattice distortion [129]. The highest reported PLQY for ultrathin $CsPbBr_3$ NWs reached 77%, with a cyan emission peak at 496 nm, accompanied by a shoulder peak at 500 nm, indicating possible impurities or aggregations in the sample [47]. However, as the NW diameter further decreases, the PLQY often drops significantly due to increased surface defects as evidenced by the shortened PL lifetimes, indicating an increase in nonradiative decay processes in thinner NWs [47, 86, 130, 131]. Additionally, optical properties of ultrathin MHP NWs can be tuned by changing the halide composition from Cl to Br to I, resulting in a PL peak shift from ultraviolet to red [30, 56, 60]. This trend is analogous to that observed in MHP perovskite nanocubes [8, 71]. Besides optical property characterizations, in 2020, Stern et al. advanced the study of ultrathin MHP NWs by applying conductive AFM technique to measure the electrical conductivity of individual ultrathin $CsPbBr_3$ and $CsPbBr_xI_{1-x}$ NWs [132]. They found that for ultrathin $CsPbBr_3$ NWs, compared to the results gained from mixed-halide NWs, the measured *I–V* curves exhibited higher currents and a steeper curve slope, indicating the presence of deeper trap-states after halide mixing. Additionally, the average rise-voltage for pure-bromide NWs was also significantly lower, suggesting more crystalline defects in $CsPbBr_xI_{1-x}$ NWs. Interestingly, the NW conductivity increased after the addition of iodide ions due to its larger atomic diameter and lower electron affinity [132]. Their study provided the first electrical characterizations of single ultrathin NWs and offered insights into the effects of anion exchange within ultrathin MHP NWs.

Building on these unique electrical and optical properties, ultrathin MHP NWs have shown promise in LED applications [38, 133, 134]. Fu et al., for instance, fabricated blue perovskite LEDs (PeLEDs) using ultrathin $CsPbBr_3$ NW arrays synthesized through an AAO template-based method [86]. The current density–voltage–luminance (*J–V–L*) curves for the resulting PeLEDs revealed that turn-on voltages increased with enlarging the bandgap of the NWs (Fig. 7(a)), while working current density decreased at the same driving voltage [86]. This phenomenon was attributed to hindered electron tunneling caused by the large $Al_2O_3$ barrier and lower carrier density in the ultrathin NWs [135, 136]. The maximum luminance achieved by these NW-based PeLEDs reached 96 cd/m$^2$ (cyan), 47 cd/m$^2$ (sky-blue), 13 cd/m$^2$ (blue), operating at 6.5, 6.8, and 7 V, with corresponding external quantum efficiencies (EQEs) of 7.1%, 3.2%, 0.9%, respectively (Fig. 7(b)). The reduced performances in the latter two devices were attributed to increased surface defects caused by a geometry mismatch between circular pores and the cubic phase perovskites of the applied ultrathin NWs [86].

Due to their anisotropic geometry and quantum confinement effects, ultrathin MHP NWs also exhibit unique polarized optical and optoelectronic properties [49, 137, 138]. When excited with linearly polarized light, NW solutions usually display a polarized PL behavior [131, 139–141]. Leveraging this property, Wang et al. fabricated a linearly polarized light detector using ultrathin $CsPbBr_3$ NWs through a brushing-assembled film method (Fig. 7(c)) [49]. The device showed its highest absorption coefficient and emission ratio when the electric field of the light was aligned parallel to the NW's axial direction (Fig. 7(d)), contrasting with the lowest value when aligned radially [49]. Upon excitation, the photocurrent

**Table 1** Summary table of reported synthesis of ultrathin $CsPbBr_3$ NWs

| Crystal phase | Abs. peak (nm) | PL peak (nm) | PL FWHM (nm) | Average PL lifetime (ns) | PLQY (%) | Synthetic method | Application | Average diameter (nm) | Reference(s) |
|---|---|---|---|---|---|---|---|---|---|
| Orthorhombic | 484 | 496 | 16 | 4.9 | 77 | Hot injection | | 5.1 ± 0.5 | [47] |
| Orthorhombic | 472 | 481, 491 | 18 | 2.8 | 40 | Hot injection | | 4.1 ± 0.7 | [47] |
| Orthorhombic | 455, 467 | 473, 483 | 33 | 2.5 | 30 | Hot injection | | 3.4 ± 0.5 | [47] |
| | 442 | 465 | 26 | | 30 | Hot injection | | 2.2 ± 0.2 | [30] |
| Orthorhombic | 445 | 460 | | | | Solvothermal | | 2.6 | [91] |
| Cubic | 420 | 430 | | | < 1 | RT colloidal synthesis | | 1.5 ± 0.5 | [63] |
| Cubic | 444 | 465 | | | 21.13 | Post-synthetic heat treatment | | 3.1 ± 0.6 | [63] |
| Orthorhombic | 427 | 445 | 23.7 | | | LARP | | | [59] |
| Orthorhombic | 441 | 454 | 22.6 | | | LARP | | 2.6 | [59] |
| Orthorhombic | 454 | 462 | 16.2 | | | LARP | | 6.1 | [59] |
| Orthorhombic | ~ 450 | 475 | | | | LARP | | ~ 3 | [56] |
| | 433 | 447 | 27 | | 60 | Post-synthetic treatment | | 2.1 | [73] |
| Orthorhombic | 413, 448 | 509 | | | 60 | LARP | | 3.8 ± 0.1 | [60] |
| Orthorhombic | 413, 448 | 498 | | | 47 | LARP | | 3.8 ± 0.1 | [60] |
| | | 433, 457 | | | | Template-assembled | | 2 | [85] |
| | 426 | 432 | ~ 12 | 7.1 | 15.2 | Post-synthetic treatment | | 2.5 ± 0.6 | [75] |
| Cubic | ~ 450 | ~ 460 | | | | RT colloidal synthesis | Linear polarized light detector | 2–3 | [49] |
| Cubic | | 467 | | 1.4 | 4 | Template-assembled | PeLED | 2.9 | [86] |
| Cubic | | 481 | | 1.967 | 16 | Template-assembled | PeLED | 3.5 | [86] |
| Cubic | | 492 | | 3.34 | 27 | Template-assembled | PeLED | 4.3 | [86] |
| Cubic | ~ 425 | ~ 450 | | | | LARP | PSCs | 2.5 ± 0.5 | [147] |

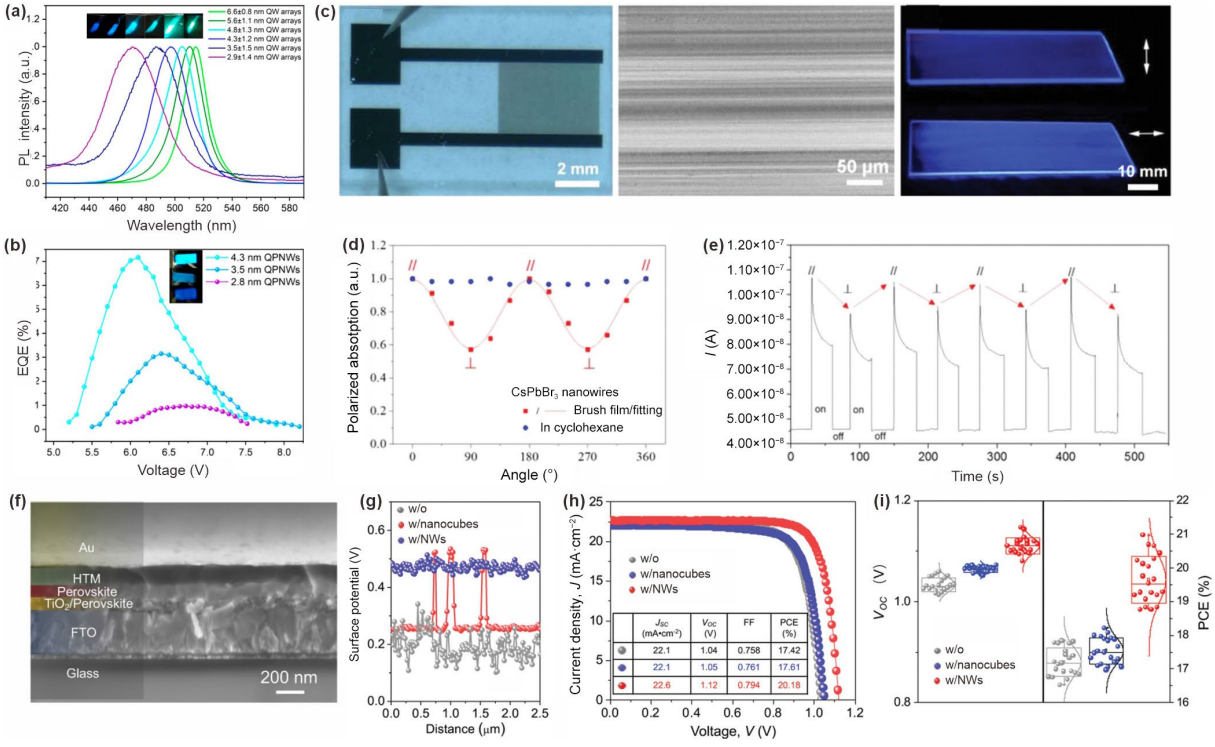


**Figure 7** (a) PL spectra of $CsPbBr_3$ QW arrays with different thicknesses. (b) EQE curves as a function of driving voltage for the QW array based PeLEDs. Reproduced with permission from Ref. [86], © American Chemical Society 2022. (c) The interdigital electrode to measure polarized optoelectronic properties (left). SEM image of the assembled ultrathin $CsPbBr_3$ NW film prepared by brushing (middle) and corresponding PL image (right). (d) The polarized absorption intensities. (e) The performance of ultrathin $CsPbBr_3$ NW film-based polarization-sensitive photodetector. Reproduced with permission from Ref. [49], © Wiley-VCH GmbH 2021. (f) Cross-sectional SEM image of the PSC using ultrathin $CsPbBr_3$ NW incorporated $MAPbI_3$ thin film. (g) The surface potential variation obtained from kelvin-probe force microscopy (KPFM) surface potential mappings of the $MAPbI_3$ thin films without NC (w/o), with $CsPbBr_3$ nanocube, and with ultrathin $CsPbBr_3$ NW incorporation. (h) *J*–*V* curves (reverse scan) and (i) PCE statistics of the corresponding PSCs. Reproduced with permission from Ref. [147], © WILEY-VCH Verlag GmbH & Co. KGaA, Weinheim 2019.

increased instantly, then decreased as charge carriers were captured by trap states in the NWs, eventually stabilized after all these trap states were filled (Fig. 7(e)) [49]. At the "light-off" edge, the photocurrent exhibited a slight increase before dropping back instantly to a stable dark current (Fig. 7(e)), indicating a quick release of the captured charge carriers. This device possessed a response rise time of 0.36 s and a fall time of 0.24 s [49]. While the direction of polarized excitation light only influenced the photocurrent intensity, the response time remained constant. Although the initial photocurrent signal was lower than other polarization-sensitive photodetectors, this method facilitates easy casting of NWs onto various substrates, making it ideal for fabricating flexible optoelectronic devices [49]. Furthermore, integrating these NWs with other hybrid nanomaterials, such as ZnO NWs, silica NWs, and polymers, could potentially enhance sensitivity and broaden the responsive wavelength range of ultrathin MHP NW-based photodetector devices [142–148].

Moreover, the superior optoelectronic properties of MHP materials make them highly promising for solar cell applications [149–151]. For thin-film perovskite solar cells (PSCs), a planar heterojunction typically forms at the interface between the hole-transporting layer (HTL) and the perovskite layer, which can create energy level mismatches that result in considerable energy loss [152–154]. In 2019, Zhang et al. demonstrated the incorporation of ultrathin $CsPbBr_3$ NWs into a methylammonium lead triiodide ($MAPbI_3$) perovskite thin-film PSC (Fig. 7(f)) [147]. It was shown that these incorporated NWs can modify the surface electronic states of the $MAPbI_3$ perovskite thin film by forming a compositionally graded heterojunction at the perovskite-HTL interface. Furthermore, the ultrathin NWs also acted as a "grating" to enhance light harvesting and energy transfer at the interface. Importantly, the NW morphology was found to be the key parameter to achieve a laterally uniform film surface, as evidenced by surface-potential mappings (Fig. 7(g)). This NW incorporation lead to an increase in the valence band maximum and boosted the device open-circuit voltage ($V_{OC}$) from 1.04 to 1.12 V—a much larger improvement than the 0.01 V increase observed with $CsPbBr_3$ perovskite nanocube incorporation (Figs. 7(h) and 7(i)) [147]. Consequently, the power conversion efficiency (PCE) of the device increased from 17.42% to 20.18% (Figs. 7(h) and 7(i)), showcasing a promising strategy for further improving PSC performance.

## 5 Summary and perspectives

In this review, we provide an overview of the advancements in the synthesis, characterization, and properties of ultrathin MHP NWs. Adding to the advantages of MHP materials, the high aspect ratio and anisotropic quantum confinement effects of ultrathin perovskite NWs make this special category of nanomaterials highly promising for both fundamental research and next-generation technological applications. However, such excitement has been held because several critical research areas remain underexplored,

despite the exciting progress made in the field. Here, we outline several critical future directions for advancing ultrathin MHP NWs toward realization of their full potential in diverse applications.

### 5.1 Controlling NW thickness at the atomic level precision

Achieving precise control over the diameter of ultrathin NWs is crucial, as their optical and electronic properties are highly sensitive to slight variations in size, particularly in the quantum-confined regime. Existing synthesis methods, while effective in producing a wide range of NW sizes, often result in inconsistencies, with discrepancies between NW sizes as observed through TEM images and their corresponding absorption peaks (Table 1). Addressing this challenge requires novel synthesis strategies capable of achieving atomic-level precision in controlling NW diameters and maintaining uniformity across large batches. By refining the synthesis process, researchers can better harness and precisely control the optical and optoelectronic properties in NWs for applications on demand.

### 5.2 Understanding growth kinetics and formation mechanisms

Despite advancements in ultrathin NW synthesis, the underlying growth mechanisms remain insufficiently understood. Unlike the synthesis of conventional semiconductor NCs with a more covalent bond character, the ionic nature of perovskites leads to their rapid formation, making it difficult to monitor nucleation and growth stages, which are key to controlling their final structure and properties. A clearer understanding of the kinetic processes governing the growth of ultrathin NWs will be critical for achieving consistent results and developing methods for fine-tuning their properties. Such studies can be possibly enabled by *in situ* monitoring tools such as electron microscopy, time-resolved spectroscopy, and X-ray scattering techniques [97, 155–159]. These mechanistic studies should focus on disentangling the factors that influence NW growth, such as temperature, ligand types, precursor composition and concentration, and solvent environment. By better understanding these processes, researchers could unlock more reliable and scalable production of NWs with finely tuned property characteristics.

### 5.3 Improving stability and environmental resistance

The thermodynamically unfavored morphology of NWs, adding to the intrinsic instability of perovskites, particularly under environmental stressors such as moisture, oxygen, and light, poses a significant barrier to the widespread use of ultrathin NWs in practical applications [48, 49, 160]. Research efforts are needed to focus on developing robust passivation techniques, such as ligand engineering, inorganic encapsulation, or core–shell heterostructure formation, to shield NWs from environmental degradation. In this context, surface modification methods, that have shown promise in enhancing the stability of other types of perovskite nanostructures [161–165], should be adapted and specifically optimized for ultrathin NWs. In addition, novel and more effective passivation strategies should be anticipated upon accumulating knowledge and understandings of the MHP NWs and perovskite materials as general in the field. The goal should be set to achieve ultrathin NWs that maintain their high performance over sufficient periods, making them viable for real-life applications such as solar cells and displays under desired working environments.

### 5.4 Expanding compositional space to nontoxic alternatives

The demand for more environmentally friendly materials has pushed researchers to explore alternatives to lead-based perovskites [19, 166–168]. Although lead-halide perovskites offer outstanding optoelectronic properties, their toxicity presents environmental and health concerns. As a result, there is growing interest in lead-free perovskite nanomaterials, including tin-, copper-, bismuth-, and antimony-based systems [23, 24, 81, 169–178]. It is well-known that these lead-free perovskite and perovskite-analogue nanomaterials can offer unique properties, such as tunable bandgaps and band structures, higher stability, along with largely reduced toxicity, making them promising candidates for future applications. Along the line, expanding the family of ultrathin perovskite NWs to include lead-free options should stand as another research focus in the field. This will not only address the lead-induced health and environmental concerns, but also open the door to the creation of new materials, for example, alloyed and/or heterostructure NWs with even wider and more precise tunability in both morphology and properties. These new materials could find applications in diverse fields such as catalysis, sensing, and energy storage, in addition to optoelectronics.

### 5.5 Exploring unique properties of ultrathin MHP NWs

Ultrathin MHP NWs exhibit distinctive properties that differentiate them from their bulk or thicker counterparts, yet many of these remain underexplored due to their current poor stability. In particular, mechanical properties, such as flexibility, tensile strength and fracture behavior, are critical for applications of NWs in flexible and wearable devices, as well as their integration into mechanical and optoelectronic systems [179–181]. However, these properties of ultrathin MHP NWs have received limited attention to date. Understanding their elasticity index, strength index and plasticity index remains elusive. Bridging this knowledge gap is essential for evaluating the mechanical robustness and deformation behaviors of ultrathin MHP NWs, thereby enabling their practical applications. In addition, the nonlinear optical properties of ultrathin NWs hold significant promise [137, 182–184]. Phenomena such as second-harmonic generation and multiphoton absorption/emission might be enhanced by the quantum confinement effects present in ultrathin geometries [185]. While thicker perovskite NWs have demonstrated nonlinear behaviors, ultrathin MHP NWs are likely to exhibit novel or amplified effects, expanding their potential for photonic devices, optical signal processing, and imaging applications [186, 187]. Moreover, lasing properties of ultrathin MHP NWs remain largely unexplored, with thicker counterparts receiving the primary focus [26, 188]. Ultrathin NWs could potentially enable low-threshold lasing, single-mode emission, or even tunable lasing behaviors owing to their distinct optical and electronic characteristics [189, 190].

In summary, ultrathin MHP NWs represent an exciting frontier in nanomaterial research, offering unique opportunities for a wide range of applications. However, challenges remain in terms of precise synthesis, mechanism understanding, materials' stability, and compositional expanding. Addressing these challenges through innovative and dedicated research will unlock the full potential of ultrathin perovskite NWs, leading to breakthroughs in their

applications in optoelectronics, energy harvesting, catalysis, and beyond. By focusing on these key research directions, it is highly anticipated that researchers can overcome current limitations and drive future innovations in this promising field.

## Data availability

All data needed to support the conclusions in the paper are presented in the manuscript. Additional data related to this paper may be requested from the corresponding author upon request.

## Acknowledgements

O. C. gratefully acknowledges the financial support from National Science Foundation under Award No. CHE-2203700.

## Declaration of competing interest

All the contributing authors report no conflict of interests in this work.

## Author contributions

Y. L. and O. C. proposed the review topic and designed the conceptual framework of the manuscript, Y. L. and Z. Z. performed the literature research and analyzed the relevant data, Y. L. and O. C. drafted and revised the manuscript, Z. L. and Z. Z. participated in the discussion and helped the manuscript revision. O. C. supervised the project.

## Use of AI statement

During the preparation of this work, the author, Y. L., used OpenAI' s ChatGPT to refine some sentences and enhance the clarity and coherence of the manuscript. After using this tool, the authors thoroughly reviewed and edited the content to ensure accuracy and originality, and take full responsibility for the final version of the publication.

## References

[1] Dey, A.; Ye, J. Z.; De, A.; Debroye, E.; Ha, S. K.; Bladt, E.; Kshirsagar, A. S.; Wang, Z. Y.; Yin, J.; Wang, Y. et al. State of the art and prospects for halide perovskite nanocrystals. *ACS Nano* **2021**, *15*, 10775–10981.

[2] Kovalenko, M. V.; Protesescu, L.; Bodnarchuk, M. I. Properties and potential optoelectronic applications of lead halide perovskite nanocrystals. *Science* **2017**, *358*, 745–750.

[3] Akkerman, Q. A.; Rainò, G.; Kovalenko, M. V.; Manna, L. Genesis, challenges and opportunities for colloidal lead halide perovskite nanocrystals. *Nat. Mater.* **2018**, *17*, 394–405.

[4] Swarnkar, A.; Chulliyil, R.; Ravi, V. K.; Irfanullah, M.; Chowdhury, A.; Nag, A. Colloidal $CsPbBr_3$ perovskite nanocrystals: Luminescence beyond traditional quantum dots. *Angew. Chem.* **2015**, *127*, 15644–15648.

[5] Shamsi, J.; Urban, A. S.; Imran, M.; De Trizio, L.; Manna, L. Metal halide perovskite nanocrystals: Synthesis, post-synthesis modifications, and their optical properties. *Chem. Rev.* **2019**, *119*, 3296–3348.

[6] Huang, H.; Bodnarchuk, M. I.; Kershaw, S. V.; Kovalenko, M. V.; Rogach, A. L. Lead halide perovskite nanocrystals in the research spotlight: Stability and defect tolerance. *ACS Energy Lett.* **2017**, *2*, 2071–2083.

[7] De Roo, J.; Ibáñez, M.; Geiregat, P.; Nedelcu, G.; Walravens, W.; Maes, J.; Martins, J. C.; Van Driessche, I.; Kovalenko, M. V.; Hens, Z. Highly dynamic ligand binding and light absorption coefficient of cesium lead bromide perovskite nanocrystals. *ACS Nano* **2016**, *10*, 2071–2081.

[8] Akkerman, Q. A.; D'Innocenzo, V.; Accornero, S.; Scarpellini, A.; Petrozza, A.; Prato, M.; Manna, L. Tuning the optical properties of cesium lead halide perovskite nanocrystals by anion exchange reactions. *J. Am. Chem. Soc.* **2015**, *137*, 10276–10281.

[9] Chen, Q. S.; Wu, J.; Ou, X. Y.; Huang, B. L.; Almutlaq, J.; Zhumekenov, A. A.; Guan, X. W.; Han, S. Y.; Liang, L. L.; Yi, Z. G. et al. All-inorganic perovskite nanocrystal scintillators. *Nature* **2018**, *561*, 88–93.

[10] Y. H.; Kim, S.; Kakekhani, A.; Park, J.; Park, J.; Lee, Y. H.; Xu, H. X.; Nagane, S.; Wexler, R. B.; Kim, D. H. et al. Comprehensive defect suppression in perovskite nanocrystals for high-efficiency light-emitting diodes. *Nat. Photonics* **2021**, *15*, 148–155.

[11] Ye, J. Z.; Byranvand, M. M.; Martínez, C. O.; Hoye, R. L. Z.; Saliba, M.; Polavarapu, L. Defect passivation in lead-halide perovskite nanocrystals and thin films: Toward efficient LEDs and solar cells. *Angew. Chem.* **2021**, *133*, 21804–21828.

[12] Hassan, Y.; Park, J. H.; Crawford, M. L.; Sadhanala, A.; Lee, J.; Sadighian, J. C.; Mosconi, E.; Shivanna, R.; Radicchi, E.; Jeong, M. et al. Ligand-engineered bandgap stability in mixed-halide perovskite LEDs. *Nature* **2021**, *591*, 72–77.

[13] Song, J. Z.; Li, J. H.; Li, X. M.; Xu, L. M.; Dong, Y. H.; Zeng, H. B. Quantum dot light-emitting diodes based on inorganic perovskite cesium lead halides ($CsPbX_3$). *Adv. Mater.* **2015**, *27*, 7162–7167.

[14] Yakunin, S.; Protesescu, L.; Krieg, F.; Bodnarchuk, M. I.; Nedelcu, G.; Humer, M.; De Luca, G.; Fiebig, M.; Heiss, W.; Kovalenko, M. V. Low-threshold amplified spontaneous emission and lasing from colloidal nanocrystals of caesium lead halide perovskites. *Nat. Commun.* **2015**, *6*, 8056.

[15] Yang, H. J.; Zhang, Y.; Hills-Kimball, K.; Zhou, Y. Y.; Chen, O. Building bridges between halide perovskite nanocrystals and thin-film solar cells. *Sustainable Energy Fuels* **2018**, *2*, 2381–2397.

[16] Wang, J. Y.; Cai, T.; Chen, O. Cesium copper halide perovskite nanocrystal-based photon-managing devices for enhanced ultraviolet photon harvesting. *Nano Lett.* **2023**, *23*, 4367–4374.

[17] Bekenstein, Y.; Koscher, B. A.; Eaton, S. W.; Yang, P. D.; Alivisatos, A. P. Highly luminescent colloidal nanoplates of perovskite cesium lead halide and their oriented assemblies. *J. Am. Chem. Soc.* **2015**, *137*, 16008–16011.

[18] R.; Gold-Parker, A.; Proppe, A. H.; Munir, R.; Yang, Z. Y.; Kelley, S. O.; Amassian, A.; Toney, M. F.; Sargent, E. H. Compositional and orientational control in metal halide perovskites of reduced dimensionality. *Nat. Mater.* **2018**, *17*, 900–907.

[19] Zhou, C. K.; Lin, H. R.; He, Q. Q.; Xu, L. J.; Worku, M.; Chaaban, M.; Lee, S.; Shi, X. Q.; Du, M. H.; Ma, B. W. Low dimensional metal halide perovskites and hybrids. *Mater. Sci. Eng. R: Rep.* **2019**, *137*, 38–65.

[20] Otero-Martínez, C.; Ye, J. Z.; Sung, J.; Pastoriza-Santos, I.; Pérez-Juste, J.; Xia, Z. G.; Rao, A.; Hoye, R. L.; Polavarapu, L. Colloidal metal-halide perovskite nanoplatelets: Thickness-controlled synthesis, properties, and application in light-emitting diodes. *Adv. Mater.* **2022**, *34*, 2107105.

[21] Bera, S.; Shyamal, S.; Pradhan, N. Chemically spiraling $CsPbBr_3$ perovskite nanorods. *J. Am. Chem. Soc.* **2021**, *143*, 14895–14906.

[22] Dong, Y. T.; Qiao, T.; Kim, D.; Parobek, D.; Rossi, D.; Son, D. H. Precise control of quantum confinement in cesium lead halide perovskite quantum dots via thermodynamic equilibrium. *Nano Lett.* **2018**, *18*, 3716–3722.

[23] Liu, Z. Y.; Yang, H. J.; Wang, J. Y.; Yuan, Y. C.; Hills-Kimball, K.; Cai, T.; Wang, P.; Tang, A. W.; Chen, O. Synthesis of lead-free $Cs_2AgBiX_6$ (X = Cl, Br, I) double perovskite nanoplatelets and their application in $CO_2$ photocatalytic reduction. *Nano Lett.* **2021**, *21*, 1620–1627.

[24] Liu, Z. Y.; Sun, Y. Y.; Cai, T.; Yang, H. J.; Zhao, J. X.; Yin, T.; Hao, C. Q.; Chen, M. J.; Shi, W. W.; Li, X. X. et al. Two-dimensional $Cs_2AgIn_xBi_{1-x}Cl_6$ alloyed double perovskite nanoplatelets for solution-processed light-emitting diodes. *Adv. Mater.* **2023**, *35*, 2211235.

[25] Zhang, D. D.; Eaton, S. W.; Yu, Y.; Dou, L. T.; Yang, P. D. Solution-phase synthesis of cesium lead halide perovskite nanowires. *J. Am. Chem. Soc.* **2015**, *137*, 9230–9233.

[26] Schlaus, A. P.; Spencer, M. S.; Miyata, K.; Liu, F.; Wang, X. X.; Datta, I.; Lipson, M.; Pan, A. L.; Zhu, X. Y. How lasing happens in $CsPbBr_3$ perovskite nanowires. *Nat. Commun.* **2019**, *10*, 265.

[27] Shoaib, M.; Zhang, X. H.; Wang, X. X.; Zhou, H.; Xu, T.; Wang, X.; Hu, X. L.; Liu, H. W.; Fan, X. P.; Zheng, W. H. et al. Directional growth of ultralong $CsPbBr_3$ perovskite nanowires for high-performance photodetectors. *J. Am. Chem. Soc.* **2017**, *139*, 15592–15595.

[28] Eaton, S. W.; Lai, M. L.; Gibson, N. A.; Wong, A. B.; Dou, L. T.; Ma, J.; Wang, L. W.; Leone, S. R.; Yang, P. D. Lasing in robust cesium lead halide perovskite nanowires. *Proc. Natl. Acad. Sci. USA* **2016**, *113*, 1993–1998.

[29] Zhu, H. M.; Fu, Y. P.; Meng, F.; Wu, X. X.; Gong, Z. Z.; Ding, Q.; Gustafsson, M. V.; Trinh, M. T.; Jin, S.; Zhu, X. Y. Lead halide perovskite nanowire lasers with low lasing thresholds and high quality factors. *Nat. Mater.* **2015**, *14*, 636–642.

[30] Zhang, D. D.; Yu, Y.; Bekenstein, Y.; Wong, A. B.; Alivisatos, A. P.; Yang, P. D. Ultrathin colloidal cesium lead halide perovskite nanowires. *J. Am. Chem. Soc.* **2016**, *138*, 13155–13158.

[31] Protesescu, L.; Yakunin, S.; Bodnarchuk, M. I.; Krieg, F.; Caputo, R.; Hendon, C. H.; Yang, R. X.; Walsh, A.; Kovalenko, M. V. Nanocrystals of cesium lead halide perovskites ($CsPbX_3$, X = Cl, Br, and I): Novel optoelectronic materials showing bright emission with wide color gamut. *Nano Lett.* **2015**, *15*, 3692–3696.

[32] Zhu, H.; Sverko, T.; Zhang, J. Y.; Berkinsky, D. B.; Sun, W. W.; Krajewska, C. J.; Bawendi, M. G. One-dimensional highly-confined $CsPbBr_3$ nanorods with enhanced stability: Synthesis and spectroscopy. *Nano Lett.* **2022**, *22*, 8355–8362.

[33] Im, J. H.; Luo, J. S.; Franckevičius, M.; Pellet, N.; Gao, P.; Moehl, T.; Zakeeruddin, S. M.; Nazeeruddin, M. K.; Grätzel, M.; Park, N. G. Nanowire perovskite solar cell. *Nano Lett.* **2015**, *15*, 2120–2126.

[34] Xia, Y.; Yang, P.; Sun, Y.; Wu, Y.; Mayers, B.; Gates, B.; Yin, Y.; Kim, F.; Yan, H. One-dimensional nanostructures: Synthesis, characterization, and applications. *Adv. Mater.* **2003**, *15*, 353–389.

[35] Zhang, D. Q.; Zhang, Q. P.; Zhu, Y. Y.; Poddar, S.; Zhang, Y. T.; Gu, L. L.; Zeng, H. B.; Fan, Z. Y. Metal halide perovskite nanowires: Synthesis, integration, properties, and applications in optoelectronics. *Adv. Energy Mater.* **2023**, *13*, 2201735.

[36] Liu, X. H.; Yu, D. J.; Song, X. F.; Zeng, H. B. Metal halide perovskites: Synthesis, ion migration, and application in field-effect transistors. *Small* **2018**, *14*, 1801460.

[37] Goldberger, J.; Hochbaum, A. I.; Fan, R.; Yang, P. D. Silicon vertically integrated nanowire field effect transistors. *Nano Lett.* **2006**, *6*, 973–977.

[38] Bi, C. H.; Hu, J. C.; Yao, Z. W.; Lu, Y.; Binks, D.; Sui, M.; Tian, J. J. Self-assembled perovskite nanowire clusters for high luminance red light-emitting diodes. *Adv. Funct. Mater.* **2020**, *30*, 2005990.

[39] Zhang, Q. P.; Zhang, D. Q.; Gu, L. L.; Tsui, K. H.; Poddar, S.; Fu, Y.; Shu, L.; Fan, Z. Y. Three-dimensional perovskite nanophotonic wire array-based light-emitting diodes with significantly improved efficiency and stability. *ACS Nano* **2020**, *14*, 1577–1585.

[40] Feng, J. G.; Gong, C.; Gao, H. F.; Wen, W.; Gong, Y. J.; Jiang, X. Y.; Zhang, B.; Wu, Y. C.; Wu, Y. S.; Fu, H. B. et al. Single-crystalline layered metal-halide perovskite nanowires for ultrasensitive photodetectors. *Nat. Electron.* **2018**, *1*, 404–410.

[41] Wang, H.; Kim, D. H. Perovskite-based photodetectors: Materials and devices. *Chem. Soc. Rev.* **2017**, *46*, 5204–5236.

[42] Gu, L. L.; Poddar, S.; Lin, Y. J.; Long, Z. H.; Zhang, D. Q.; Zhang, Q. P.; Shu, L.; Qiu, X.; Kam, M.; Javey, A. et al. A biomimetic eye with a hemispherical perovskite nanowire array retina. *Nature* **2020**, *581*, 278–282.

[43] Gu, L. L.; Tavakoli, M. M.; Zhang, D. Q.; Zhang, Q. P.; Waleed, A.; Xiao, Y. Q.; Tsui, K. H.; Lin, Y. J.; Liao, L.; Wang, J. N. et al. 3D arrays of 1024-pixel image sensors based on lead halide perovskite nanowires. *Adv. Mater.* **2016**, *28*, 9713–9721.

[44] Gong, S.; Schwalb, W.; Wang, Y. W.; Chen, Y.; Tang, Y.; Si, J.; Shirinzadeh, B.; Cheng, W. L. A wearable and highly sensitive pressure sensor with ultrathin gold nanowires. *Nat. Commun.* **2014**, *5*, 3132.

[45] Koenigsmann, C.; Santulli, A. C.; Gong, K. P.; Vukmirovic, M. B.; Zhou, W. P.; Sutter, E.; Wong, S. S.; Adzic, R. R. Enhanced electrocatalytic performance of processed, ultrathin, supported Pd–Pt core–shell nanowire catalysts for the oxygen reduction reaction. *J. Am. Chem. Soc.* **2011**, *133*, 9783–9795.

[46] Xia, B. Y.; Wu, H. B.; Yan, Y.; Lou, X. W.; Wang, X. Ultrathin and ultralong single-crystal platinum nanowire assemblies with highly stable electrocatalytic activity. *J. Am. Chem. Soc.* **2013**, *135*, 9480–9485.

[47] M.; Di Stasio, F.; Dang, Z. Y.; Canale, C.; Khan, A. H.; Shamsi, J.; Brescia, R.; Prato, M.; Manna, L. Colloidal synthesis of strongly fluorescent $CsPbBr_3$ nanowires with width tunable down to the quantum confinement regime. *Chem. Mater.* **2016**, *28*, 6450–6454.

[48] Di Stasio, F.; Imran, M.; Akkerman, Q. A.; Prato, M.; Manna, L.; Krahne, R. Reversible concentration-dependent photoluminescence quenching and change of emission color in $CsPbBr_3$ nanowires and nanoplatelets. *J. Phys. Chem. Lett.* **2017**, *8*, 2725–2729.

[49] Wang, Y. K.; Liu, X. Y.; He, Q. Q.; Chen, G. Y.; Xu, D. D.; Chen, X. D.; Zhao, W. B.; Bao, J. C.; Xu, X. X.; Liu, J. L. et al. Reversible transformation between $CsPbBr_3$ perovskite nanowires and nanorods with polarized optoelectronic properties. *Adv. Funct. Mater.* **2021**, *31*, 2011251.

[50] Ko, S. H.; Pan, H.; Grigoropoulos, C. P.; Luscombe, C. K.; Fréchet, J. M. J.; Poulikakos, D. All-inkjet-printed flexible electronics fabrication on a polymer substrate by low-temperature high-resolution selective laser sintering of metal nanoparticles. *Nanotechnology* **2007**, *18*, 345202.

[51] Yang, D.; Yang, R. X.; Priya, S.; Liu, S. Z. Recent advances in flexible perovskite solar cells: Fabrication and applications. *Angew. Chem., Int. Ed.* **2019**, *58*, 4466–4483.

[52] You, J. B.; Hong, Z. R.; Yang, Y.; Chen, Q.; Cai, M.; Song, T. B.; Chen, C. C.; Lu, S. R.; Liu, Y. S.; Zhou, H. P. et al. Low-temperature solution-processed perovskite solar cells with high efficiency and flexibility. *ACS Nano* **2014**, *8*, 1674–1680.

[53] Zhang, F.; Zhong, H. Z.; Chen, C.; Wu, X. G.; Hu, X. M.; Huang, H. L.; Han, J. B.; Zou, B. S.; Dong, Y. P. Brightly luminescent and color-tunable colloidal $CH_3NH_3PbX_3$ (X = Br, I, Cl) quantum dots: Potential alternatives for display technology. *ACS Nano* **2015**, *9*, 4533–4542.

[54] Huang, H.; Susha, A. S.; Kershaw, S. V.; Hung, T. F.; Rogach, A. L. Control of emission color of high quantum yield $CH_3NH_3PbBr_3$ perovskite quantum dots by precipitation temperature. *Adv. Sci.* **2015**, *2*, 1500194.

[55] Kulkarni, S. A.; Mhaisalkar, S. G.; Mathews, N.; Boix, P. P. Perovskite nanoparticles: Synthesis, properties, and novel applications in photovoltaics and LEDs. *Small Methods* **2019**, *3*, 1800231.

[56] Amgar, D.; Stern, A.; Rotem, D.; Porath, D.; Etgar, L. Tunable length and optical properties of $CsPbX_3$ (X = Cl, Br, I) nanowires with a few unit cells. *Nano Lett.* **2017**, *17*, 1007–1013.

[57] Sichert, J. A.; Tong, Y.; Mutz, N.; Vollmer, M.; Fischer, S.; Milowska, K. Z.; García Cortadella, R.; Nickel, B.; Cardenas-Daw, C.; Stolarczyk, J. K. et al. Quantum size effect in organometal halide perovskite nanoplatelets. *Nano Lett.* **2015**, *15*, 6521–6527.

[58] Yuan, Z.; Shu, Y.; Tian, Y.; Xin, Y.; Ma, B. W. A facile one-pot

synthesis of deep blue luminescent lead bromide perovskite microdisks. *Chem. Commun.* **2015**, *51*, 16385–16388.

[59] Kostopoulou, A.; Sygletou, M.; Brintakis, K.; Lappas, A.; Stratakis, E. Low-temperature benchtop-synthesis of all-inorganic perovskite nanowires. *Nanoscale* **2017**, *9*, 18202–18207.

[60] He, L. Z.; Pan, S.; Lin, Z. Q.; Peng, J. Rapid route to polar solvent-directed growth of perovskite nanowires. *ACS Appl. Nano Mater.* **2019**, *2*, 7910–7915.

[61] Ahmed, G. H.; Yin, J.; Bose, R.; Sinatra, L.; Alarousu, E.; Yengel, E.; AlYami, N. M.; Saidaminov, M. I.; Zhang, Y. H.; Hedhili, M. N. et al. Pyridine-induced dimensionality change in hybrid perovskite nanocrystals. *Chem. Mater.* **2017**, *29*, 4393–4400.

[62] Hu, J. C.; Bi, C. H.; Zhang, X. T.; Lu, Y.; Zhou, W. C.; Zheng, Z. L.; Tang, Y.; Lu, F.; Yao, Z. W.; Tian, B. H. et al. Yellow-light emitted single halide $CsPbI_3$ nanowire. *Appl. Mater. Today.* **2022**, *29*, 101592.

[63] Huang, H. W.; Liu, M.; Li, J.; Luo, L. H.; Zhao, J. T.; Luo, Z. L.; Wang, X. P.; Ye, Z. Z.; He, H. P.; Zeng, J. Atomically thin cesium lead bromide perovskite quantum wires with high luminescence. *Nanoscale* **2017**, *9*, 104–108.

[64] Yang, H. J.; Cai, T.; Dube, L.; Chen, O. Synthesis of double perovskite and quadruple perovskite nanocrystals through post-synthetic transformation reactions. *Chem. Sci.* **2022**, *13*, 4874–4883.

[65] Paul, S.; Acharya, S. Postsynthesis transformation of halide perovskite nanocrystals. *ACS Energy Lett.* **2022**, *7*, 2136–2155.

[66] Dube, L.; Saghy, P.; Chen, O. Post-synthetic doping and ligand engineering of $Cs_2AgInCl_6$ double perovskite nanocrystals. *J. Phys. Chem. C* **2023**, *127*, 21849–21859.

[67] Debnath, G. H.; Georgieva, Z. N.; Bloom, B. P.; Tan, S. S.; Waldeck, D. H. Using post-synthetic ligand modification to imprint chirality onto the electronic states of cesium lead bromide ($CsPbBr_3$) perovskite nanoparticles. *Nanoscale* **2021**, *13*, 15248–15256.

[68] Wang, B.; Zhang, C. Y.; Huang, S. Q.; Li, Z. C.; Kong, L.; Jin, L.; Wang, J. H.; Wu, K. F.; Li, L. Postsynthesis phase transformation for $CsPbBr_3/Rb_4PbBr_6$ core/shell nanocrystals with exceptional photostability. *ACS Appl. Mater. Interfaces.* **2018**, *10*, 23303–23310.

[69] Hills-Kimball, K.; Pérez, M. J.; Nagaoka, Y.; Cai, T.; Yang, H. J.; Davis, A. H.; Zheng, W. W.; Chen, O. Ligand engineering for $Mn^{2+}$ doping control in $CsPbCl_3$ perovskite nanocrystals via a quasi-solid-solid cation exchange reaction. *Chem. Mater.* **2020**, *32*, 2489–2500.

[70] Yang, H. J.; Cai, T.; Liu, E. X.; Hills-Kimball, K.; Gao, J. B.; Chen, O. Synthesis and transformation of zero-dimensional $Cs_3BiX_6$ (X = Cl, Br) perovskite-analogue nanocrystals. *Nano Res.* **2020**, *13*, 282–291.

[71] Nedelcu, G.; Protesescu, L.; Yakunin, S.; Bodnarchuk, M. I.; Grotevent, M. J.; Kovalenko, M. V. Fast anion-exchange in highly luminescent nanocrystals of cesium lead halide perovskites ($CsPbX_3$, X = Cl, Br, I). *Nano Lett.* **2015**, *15*, 5635–5640.

[72] Wu, L. Z.; Hu, H. C.; Xu, Y.; Jiang, S.; Chen, M.; Zhong, Q. X.; Yang, D.; Liu, Q. P.; Zhao, Y.; Sun, B. Q. et al. From nonluminescent $Cs_4PbX_6$ (X = Cl, Br, I) nanocrystals to highly luminescent $CsPbX_3$ nanocrystals: Water-triggered transformation through a CsX-stripping mechanism. *Nano Lett.* **2017**, *17*, 5799–5804.

[73] Li, P. L.; Yang, D.; Tan, Y. S.; Cao, M. H.; Zhong, Q. X.; Chen, M.; Hu, H. C.; Sun, B. Q.; Xu, Y.; Zhang, Q. Consecutive interfacial transformation of cesium lead halide nanocubes to ultrathin nanowires with improved stability. *ACS Appl. Mater. Interfaces.* **2019**, *11*, 3351–3359.

[74] Bohn, B. J.; Tong, Y.; Gramlich, M.; Lai, M. L.; Döblinger, M.; Wang, K.; Hoye, R. L. Z.; Müller-Buschbaum, P.; Stranks, S. D.; Urban, A. S. et al. Boosting tunable blue luminescence of halide perovskite nanoplatelets through postsynthetic surface trap repair. *Nano Lett.* **2018**, *18*, 5231–5238.

[75] Yang, H. J.; Cai, T.; Dube, L.; Hills-Kimball, K.; Chen, O. Synthesis of ultrathin perovskite nanowires via a postsynthetic transformation reaction of zero-dimensional perovskite nanocrystals. *Cryst. Growth Des.* **2021**, *21*, 1924–1930.

[76] Huczko, A. Template-based synthesis of nanomaterials. *Appl. Phys. A* **2000**, *70*, 365–376.

[77] Wu, Y. Y.; Livneh, T.; Zhang, Y. X.; Cheng, G. S.; Wang, J. F.; Tang, J.; Moskovits, M.; Stucky, G. D. Templated synthesis of highly ordered mesostructured nanowires and nanowire arrays. *Nano Lett.* **2004**, *4*, 2337–2342.

[78] Hurst, S. J.; Payne, E. K.; Qin, L. D.; Mirkin, C. A. Multisegmented one-dimensional nanorods prepared by hard-template synthetic methods. *Angew. Chem., Int. Ed.* **2006**, *45*, 2672–2692.

[79] Cao, G. Z.; Liu, D. W. Template-based synthesis of nanorod, nanowire, and nanotube arrays. *Adv. Colloid Interface Sci.* **2008**, *136*, 45–64.

[80] Liu, Y. D.; Goebl, J.; Yin, Y. D. Templated synthesis of nanostructured materials. *Chem. Soc. Rev.* **2013**, *42*, 2610–2653.

[81] Luo, Z. S.; Li, Q.; Zhang, L. M.; Wu, X. T.; Tan, L.; Zou, C.; Liu, Y. J.; Quan, Z. W. 0D $Cs_3Cu_2X_5$ (X = I, Br, and Cl) nanocrystals: Colloidal syntheses and optical properties. *Small* **2020**, *16*, 1905226.

[82] Ashley, M. J.; O'Brien, M. N.; Hedderick, K. R.; Mason, J. A.; Ross, M. B.; Mirkin, C. A. Templated synthesis of uniform perovskite nanowire arrays. *J. Am. Chem. Soc.* **2016**, *138*, 10096–10099.

[83] Waleed, A.; Tavakoli, M. M.; Gu, L. L.; Wang, Z. Y.; Zhang, D. Q.; Manikandan, A.; Zhang, Q. P.; Zhang, R. J.; Chueh, Y. L.; Fan, Z. Y. Lead-free perovskite nanowire array photodetectors with drastically improved stability in nanoengineering templates. *Nano Lett.* **2017**, *17*, 523–530.

[84] Dirin, D. N.; Protesescu, L.; Trummer, D.; Kochetygov, I. V.; Yakunin, S.; Krumeich, F.; Stadie, N. P.; Kovalenko, M. V. Harnessing defect-tolerance at the nanoscale: Highly luminescent lead halide perovskite nanocrystals in mesoporous silica matrixes. *Nano Lett.* **2016**, *16*, 5866–5874.

[85] Zhang, L. H.; Sun, Q. S.; Xu, Y. K.; Han, L. L.; Wang, Q.; Yu, Y. C.; Jin, Z. W.; Yang, S. K.; Ci, Z. Self-assembled template-confined growth of ultrathin $CsPbBr_3$ nanowires. *Appl. Mater. Today* **2020**, *18*, 100449.

[86] Fu, Y.; Poddar, S.; Ren, B. T.; Xie, Y.; Zhang, Q. P.; Zhang, D. Q.; Cao, B.; Tang, Y. Q.; Ding, Y. C.; Qiu, X. et al. Strongly quantum-confined perovskite nanowire arrays for color-tunable blue-light-emitting diodes. *ACS Nano* **2022**, *16*, 8388–8398.

[87] Gao, M. Y.; Park, Y.; Jin, J. B.; Chen, P. C.; Devyldere, H.; Yang, Y.; Song, C. Y.; Lin, Z. N.; Zhao, Q. C.; Siron, M. et al. Direct observation of transient structural dynamics of atomically thin halide perovskite nanowires. *J. Am. Chem. Soc.* **2023**, *145*, 4800–4807.

[88] Puppin, M.; Polishchuk, S.; Colonna, N.; Crepaldi, A.; Dirin, D. N.; Nazarenko, O.; De Gennaro, R.; Gatti, G.; Roth, S.; Barillot, T. et al. Evidence of large polarons in photoemission band mapping of the perovskite semiconductor $CsPbBr_3$. *Phys. Rev. Lett.* **2020**, *124*, 206402.

[89] Motti, S. G.; Meggiolaro, D.; Martani, S.; Sorrentino, R.; Barker, A. J.; De Angelis, F.; Petrozza, A. Defect activity in lead halide perovskites. *Adv. Mater.* **2019**, *31*, 1901183.

[90] W.; Lin, J.; Li, C.; Hu, S. M.; Huang, Y.; Yu, C.; Wen, Z. K.; Liu, Z. Y.; Fang, Y.; Tang, C. C. Solvothermal synthesis of cesium lead halide perovskite nanowires with ultra-high aspect ratios for high-performance photodetectors. *Nanoscale* **2018**, *10*, 21451–21458.

[91] Chen, M.; Zou, Y. T.; Wu, L. Z.; Pan, Q.; Yang, D.; Hu, H. C.; Tan, Y. S.; Zhong, Q. X.; Xu, Y.; Liu, H. Y. et al. Solvothermal synthesis of high-quality all-inorganic cesium lead halide perovskite nanocrystals: From nanocube to ultrathin nanowire. *Adv. Funct. Mater.* **2017**, *27*, 1701121.

[92] Zhai, W.; Lin, J.; Li, Q. L.; Zheng, K.; Huang, Y.; Yao, Y. Z.; He, X.; Li, L. L.; Yu, C.; Liu, C. et al. Solvothermal synthesis of ultrathin cesium lead halide perovskite nanoplatelets with tunable lateral sizes and their reversible transformation into $Cs_4PbBr_6$ nanocrystals. *Chem. Mater.* **2018**, *30*, 3714–3721.

[93] Yu, M. M.; Zhang, D.; Xu, Y. B.; Lin, J.; Yu, C.; Fang, Y.; Liu, Z. Y.; Guo, Z. L.; Tang, C. C.; Huang, Y. Surface ligand engineering of $CsPbBr_3$ perovskite nanowires for high-performance photodetectors. *J. Colloid Interface Sci.* **2022**, *608*, 2367–2376.

[94] Lai, J. P.; Niu, W. X.; Luque, R.; Xu, G. B. Solvothermal synthesis of metal nanocrystals and their applications. *Nano Today* **2015**, *10*, 240–267.

[95] L. P.; Hu, Y. L.; Pelligra, C.; Chen, C. H.; Jin, L.; Huang, H.; Sithambaram, S.; Aindow, M.; Joesten, R.; Suib, S. L. ZnO with different morphologies synthesized by solvothermal methods for enhanced photocatalytic activity. *Chem. Mater.* **2009**, *21*, 2875–2885.

[96] Sun, C. W.; Li, H.; Zhang, H. R.; Wang, Z. X.; Chen, L. Q. Controlled synthesis of $CeO_2$ nanorods by a solvothermal method. *Nanotechnology* **2005**, *16*, 1454–1463.

[97] Q. A.; Nguyen, T. P. T.; Boehme, S. C.; Montanarella, F.; Dirin, D. N.; Wechsler, P.; Beiglböck, F.; Rainò, G.; Erni, R.; Katan, C. et al. Controlling the nucleation and growth kinetics of lead halide perovskite quantum dots. *Science* **2022**, *377*, 1406–1412.

[98] Gao, Q. J.; Qi, J. H.; Chen, K.; Xia, M. H.; Hu, Y.; Mei, A. Y.; Han, H. W. Halide perovskite crystallization processes and methods in nanocrystals, single crystals, and thin films. *Adv. Mater.* **2022**, *34*, 2200720.

[99] Qiao, Z.; Wang, X.; Zhai, Y. F.; Yu, R. Z.; Fang, Z.; Chen, G. *In situ* real-time observation of formation and self-assembly of perovskite nanocrystals at high temperature. *Nano Lett.* **2023**, *23*, 10788–10795.

[100] Tang, X. S.; Zu, Z. Q.; Shao, H. B.; Hu, W.; Zhou, M.; Deng, M.; Chen, W. W.; Zang, Z. G.; Zhu, T.; Xue, J. M. All-inorganic perovskite $CsPb(Br/I)_3$ nanorods for optoelectronic application. *Nanoscale* **2016**, *8*, 15158–15161.

[101] LaMer, V. K.; Dinegar, R. H. Theory, production and mechanism of formation of monodispersed hydrosols. *J. Am. Chem. Soc.* **1950**, *72*, 4847–4854.

[102] Tong, Y.; Bohn, B. J.; Bladt, E.; Wang, K.; Müller-Buschbaum, P.; Bals, S.; Urban, A. S.; Polavarapu, L.; Feldmann, J. From precursor powders to $CsPbX_3$ perovskite nanowires: One-pot synthesis, growth mechanism, and oriented self-assembly. *Angew. Chem., Int. Ed.* **2017**, *56*, 13887–13892.

[103] Liu, J. K.; Song, K. P.; Shin, Y.; Liu, X.; Chen, J.; Yao, K. X.; Pan, J.; Yang, C.; Yin, J.; Xu, L. J. et al. Light-induced self-assembly of cubic $CsPbBr_3$ perovskite nanocrystals into nanowires. *Chem. Mater.* **2019**, *31*, 6642–6649.

[104] Cho, K. S.; Talapin, D. V.; Gaschler, W.; Murray, C. B. Designing PbSe nanowires and nanorings through oriented attachment of nanoparticles. *J. Am. Chem. Soc.* **2005**, *127*, 7140–7147.

[105] Liu, L. L.; Kluherz, K.; Jin, B.; Gamelin, D. R.; De Yoreo, J. J.; Sushko, M. L. Oriented assembly of lead halide perovskite nanocrystals. *Nano Lett.* **2024**, *24*, 3299–3306.

[106] Zhang, Q.; Liu, S. J.; Yu, S. H. Recent advances in oriented attachment growth and synthesis of functional materials: Concept, evidence, mechanism, and future. *J. Mater. Chem.* **2009**, *19*, 191–207.

[107] Lv, W. Q.; He, W. D.; Wang, X. N.; Niu, Y. H.; Cao, H. Q.; Dickerson, J. H.; Wang, Z. G. Understanding the oriented-attachment growth of nanocrystals from an energy point of view: A review. *Nanoscale* **2014**, *6*, 2531–2547.

[108] Morris-Cohen, A. J.; Vasilenko, V.; Amin, V. A.; Reuter, M. G.; Weiss, E. A. Model for adsorption of ligands to colloidal quantum dots with concentration-dependent surface structure. *ACS Nano* **2012**, *6*, 557–565.

[109] Kazes, M.; Udayabhaskararao, T.; Dey, S.; Oron, D. Effect of surface ligands in perovskite nanocrystals: Extending in and reaching out. *Acc. Chem. Res.* **2021**, *54*, 1409–1418.

[110] A. Z.; He, B.; Fan, X. Y.; Liu, Z. K.; Urban, J. J.; Alivisatos, A. P.; He, L.; Liu, Y. Insight into the ligand-mediated synthesis of colloidal $CsPbBr_3$ perovskite nanocrystals: The role of organic acid, base, and cesium precursors. *ACS Nano* **2016**, *10*, 7943–7954.

[111] Luo, B. B.; Pu, Y. C.; Lindley, S. A.; Yang, Y.; Lu, L. Q.; Li, Y.; Li, X. M.; Zhang, J. Z. Organolead halide perovskite nanocrystals: Branched capping ligands control crystal size and stability. *Angew. Chem., Int. Ed.* **2016**, *55*, 8864–8868.

[112] Sun, S. B.; Yuan, D.; Xu, Y.; Wang, A. F.; Deng, Z. T. Ligand-mediated synthesis of shape-controlled cesium lead halide perovskite nanocrystals via reprecipitation process at room temperature. *ACS Nano* **2016**, *10*, 3648–3657.

[113] Dang, Z. Y.; Shamsi, J.; Palazon, F.; Imran, M.; Akkerman, Q. A.; Park, S.; Bertoni, G.; Prato, M.; Brescia, R.; Manna, L. *In situ* transmission electron microscopy study of electron beam-induced transformations in colloidal cesium lead halide perovskite nanocrystals. *ACS Nano* **2017**, *11*, 2124–2132.

[114] Zhang, D. D.; Yang, Y. M.; Bekenstein, Y.; Yu, Y.; Gibson, N. A.; Wong, A. B.; Eaton, S. W.; Kornienko, N.; Kong, Q.; Lai, M. L. et al. Synthesis of composition tunable and highly luminescent cesium lead halide nanowires through anion-exchange reactions. *J. Am. Chem. Soc.* **2016**, *138*, 7236–7239.

[115] Urban, K. W. Studying atomic structures by aberration-corrected transmission electron microscopy. *Science* **2008**, *321*, 506–510.

[116] Yu, Y.; Cui, F.; Sun, J. W.; Yang, P. D. Atomic structure of ultrathin gold nanowires. *Nano Lett.* **2016**, *16*, 3078–3084.

[117] Straus, D. B.; Guo, S.; Cava, R. J. Kinetically stable single crystals of perovskite-phase $CsPbI_3$. *J. Am. Chem. Soc.* **2019**, *141*, 11435–11439.

[118] A.; Marshall, A. R.; Sanehira, E. M.; Chernomordik, B. D.; Moore, D. T.; Christians, J. A.; Chakrabarti, T.; Luther, J. M. Quantum dot-induced phase stabilization of α-$CsPbI_3$ perovskite for high-efficiency photovoltaics. *Science* **2016**, *354*, 92–95.

[119] Pham, T.; Oh, S.; Stetz, P.; Onishi, S.; Kisielowski, C.; Cohen, M. L.; Zettl, A. Torsional instability in the single-chain limit of a transition metal trichalcogenide. *Science* **2018**, *361*, 263–266.

[120] Holder, C. F.; Schaak, R. E. Tutorial on powder X-ray diffraction for characterizing nanoscale materials. *ACS Nano* **2019**, *13*, 7359–7365.

[121] Misra, S.; Liu, N.; Nelson, J.; Hong, S. S.; Cui, Y.; Toney, M. F. *In situ* X-ray diffraction studies of (de) lithiation mechanism in silicon nanowire anodes. *ACS Nano* **2012**, *6*, 5465–5473.

[122] Zhao, J. T.; Liu, M.; Fang, L.; Jiang, S. L.; Zhou, J. T.; Ding, H. Y.; Huang, H. W.; Wen, W.; Luo, Z. L.; Zhang, Q. et al. Great disparity in photoluminesence quantum yields of colloidal $CsPbBr_3$ nanocrystals with varied shape: The effect of crystal lattice strain. *J. Phys. Chem. Lett.* **2017**, *8*, 3115–3121.

[123] Wang, Z. L. Transmission electron microscopy of shape-controlled nanocrystals and their assemblies. *J. Phys. Chem. B* **2000**, *104*, 1153–1175.

[124] Zhou, G. M.; Xu, L.; Hu, G. W.; Mai, L.; Cui, Y. Nanowires for electrochemical energy storage. *Chem. Rev.* **2019**, *119*, 11042–11109.

[125] Sun, Y. G. Silver nanowires-unique templates for functional nanostructures. *Nanoscale* **2010**, *2*, 1626–1642.

[126] Kikhney, A. G.; Svergun, D. I. A practical guide to small angle X-ray scattering (SAXS) of flexible and intrinsically disordered proteins. *FEBS Lett.* **2015**, *589*, 2570–2577.

[127] Teunis, M. B.; Jana, A.; Dutta, P.; Johnson, M. A.; Mandal, M.; Muhoberac, B. B.; Sardar, R. Mesoscale growth and assembly of bright luminescent organolead halide perovskite quantum wires. *Chem. Mater.* **2016**, *28*, 5043–5054.

[128] Stoumpos, C. C.; Malliakas, C. D.; Peters, J. A.; Liu, Z. F.; Sebastian, M.; Im, J.; Chasapis, T. C.; Wibowo, A. C.; Chung, D. Y.; Freeman, A. J. et al. Crystal growth of the perovskite semiconductor $CsPbBr_3$: A new material for high-energy radiation detection. *Cryst. Growth Des.* **2013**, *13*, 2722–2727.

[129] Zhang, D. Q.; Gu, L. L.; Zhang, Q. P.; Lin, Y. J.; Lien, D. H.; Kam, M.; Poddar, S.; Garnett, E. C.; Javey, A.; Fan, Z. Y. Increasing photoluminescence quantum yield by nanophotonic design of quantum-confined halide perovskite nanowire arrays. *Nano Lett.*

**2019**, *19*, 2850–2857.
[130] Zheng, X. P.; Hou, Y.; Sun, H. T.; Mohammed, O. F.; Sargent, E. H.; Bakr, O. M. Reducing defects in halide perovskite nanocrystals for light-emitting applications. *J. Phys. Chem. Lett.* **2019**, *10*, 2629–2640.
[131] Peng, Z. X.; Yang, D. D.; Yin, B. Z.; Guo, X.; Li, S.; Zhan, Q. Q.; Xiao, X. D.; Liu, X. F.; Xia, Z. G.; Yang, Z. M. et al. Self-assembled ultrafine $CsPbBr_3$ perovskite nanowires for polarized light detection. *Sci. China Mater* **2021**, *64*, 2261–2271.
[132] Stern, A.; Aharon, S.; Binyamin, T.; Karmi, A.; Rotem, D.; Etgar, L.; Porath, D. Electrical characterization of individual cesium lead halide perovskite nanowires using conductive AFM. *Adv. Mater.* **2020**, *32*, 1907812.
[133] Aftab, S.; Kabir, F.; Mukhtar, M.; Hussain, I.; Nazir, G.; Aslam, M.; Hegazy, H. H.; Yewale, M. A. Perovskite quantum wires: A review of their exceptional optoelectronic properties and diverse applications in revolutionary technologies. *Nano Energy* **2024**, *129*, 109995.
[134] Zhang, D. Q.; Zhu, Y. D.; Zhang, Q. P.; Ren, B. T.; Cao, B.; Li, Q. Z.; Poddar, S.; Zhou, Y.; Qiu, X.; He, Z. B. et al. Vertical heterogeneous integration of metal halide perovskite quantum-wires/nanowires for flexible narrowband photodetectors. *Nano Lett.* **2022**, *22*, 3062–3070.
[135] Gloos, K.; Koppinen, P. J.; Pekola, J. P. Properties of native ultrathin aluminium oxide tunnel barriers. *J. Phys.: Condens. Matter* **2003**, *15*, 1733–1746.
[136] Pollack, S. R.; Morris, C. F. Electron tunneling through asymmetric films of thermally grown $Al_2O_3$. *J. Appl. Phys.* **1964**, *35*, 1503–1512.
[137] Nakayama, Y.; Pauzauskie, P. J.; Radenovic, A.; Onorato, R. M.; Saykally, R. J.; Liphardt, J.; Yang, P. D. Tunable nanowire nonlinear optical probe. *Nature* **2007**, *447*, 1098–1101.
[138] Zhou, N. J.; Bekenstein, Y.; Eisler, C. N.; Zhang, D. D.; Schwartzberg, A. M.; Yang, P. D.; Alivisatos, A. P.; Lewis, J. A. Perovskite nanowire-block copolymer composites with digitally programmable polarization anisotropy. *Sci. Adv.* **2019**, *5*, eaav8141.
[139] Wang, J. F.; Gudiksen, M. S.; Duan, X. F.; Cui, Y.; Lieber, C. M. Highly polarized photoluminescence and photodetection from single indium phosphide nanowires. *Science* **2001**, *293*, 1455–1457.
[140] Lin, C. H.; Kang, C. Y.; Wu, T. Z.; Tsai, C. L.; Sher, C. W.; Guan, X. W.; Lee, P. T.; Wu, T.; Ho, C. H.; Kuo, H. C. et al. Giant optical anisotropy of perovskite nanowire array films. *Adv. Funct. Mater.* **2020**, *30*, 1909275.
[141] Shi, S.; Sun, L. D.; Xue, Y. X.; Dong, H.; Wu, K.; Guo, S. C.; Wu, B. T.; Yan, C. H. Scalable direct writing of lanthanide-doped $KMnF_3$ perovskite nanowires into aligned arrays with polarized up-conversion emission. *Nano Lett.* **2018**, *18*, 2964–2969.
[142] Wang, J. X.; Zhang, Y. Z.; Chen, J.; Wei, Y.; Yu, D. J.; Liang, L. M.; Liu, Y.; Wu, Y.; Shen, W. L.; Li, X. M. et al. Strong polarized photoluminescence $CsPbBr_3$ nanowire composite films for UV spectral conversion polarization photodetector enhancement. *ACS Appl. Mater. Interfaces.* **2021**, *13*, 36147–36156.
[143] Pan, A. Z.; Jurow, M. J.; Wu, Y. S.; Jia, M. J.; Zheng, F. Y.; Zhang, Y. F.; He, L.; Liu, Y. Highly stable luminous "snakes" from $CsPbX_3$ perovskite nanocrystals anchored on amine-coated silica nanowires. *ACS Appl. Nano Mater.* **2019**, *2*, 258–266.
[144] Jiang, Y.; Liao, J. F.; Xu, Y. F.; Chen, H. Y.; Wang, X. D.; Kuang, D. B. Hierarchical $CsPbBr_3$ nanocrystal-decorated ZnO nanowire/macroporous graphene hybrids for enhancing charge separation and photocatalytic $CO_2$ reduction. *J. Mater. Chem. A* **2019**, *7*, 13762–13769.
[145] Zhang, J. Y.; Jiao, B.; Dai, J. F.; Wu, D. M.; Wu, Z. X.; Bian, L. F.; Zhao, Y. K.; Yang, W. X.; Jiang, M.; Lu, S. L. Enhance the responsivity and response speed of self-powered ultraviolet photodetector by GaN/$CsPbBr_3$ core–shell nanowire heterojunction and hydrogel. *Nano Energy* **2022**, *100*, 107437.
[146] Lee, H. Y.; Kim, S. Nanowires for 2D material-based photonic and optoelectronic devices. *Nanophotonics* **2022**, *11*, 2571–2582.
[147] Zhang, Y.; Yang, H. J.; Chen, M.; Padture, N. P.; Chen, O.; Zhou, Y. Y. Fusing nanowires into thin films: Fabrication of graded-heterojunction perovskite solar cells with enhanced performance. *Adv. Energy Mater.* **2019**, *9*, 1900243.
[148] Gökbulut, B.; Topcu, G.; Demir, M. M.; Inci, M. N. Plasmon-induced spectral tunability of perovskite nanowires. *Opt. Mater.* **2021**, *122*, 111702.
[149] Rong, Y. G.; Hu, Y.; Mei, A. Y.; Tan, H. R.; Saidaminov, M. I.; Seok, S. I.; McGehee, M. D.; Sargent, E. H.; Han, H. W. Challenges for commercializing perovskite solar cells. *Science* **2018**, *361*, eaat8235.
[150] Green, M. A.; Ho-Baillie, A.; Snaith, H. J. The emergence of perovskite solar cells. *Nat. Photonics* **2014**, *8*, 506–514.
[151] Kim, J. Y.; Lee, J. W.; Jung, H. S.; Shin, H.; Park, N. G. High-efficiency perovskite solar cells. *Chem. Rev.* **2020**, *120*, 7867–7918.
[152] Wang, T. Y.; Deng, W. Q.; Cao, J. P.; Yan, F. Recent progress on heterojunction engineering in perovskite solar cells. *Adv. Energy Mater.* **2023**, *13*, 2201436.
[153] Wu, X.; Li, B.; Zhu, Z. L.; Chueh, C. C.; Jen, A. K. Y. Designs from single junctions, heterojunctions to multijunctions for high-performance perovskite solar cells. *Chem. Soc. Rev.* **2021**, *50*, 13090–13128.
[154] Liu, M. Z.; Johnston, M. B.; Snaith, H. J. Efficient planar heterojunction perovskite solar cells by vapour deposition. *Nature* **2013**, *501*, 395–398.
[155] Nielsen, M. H.; Aloni, S.; De Yoreo, J. J. *In situ* TEM imaging of $CaCO_3$ nucleation reveals coexistence of direct and indirect pathways. *Science* **2014**, *345*, 1158–1162.
[156] Zhou, Y. Y.; Sternlicht, H.; Padture, N. P. Transmission electron microscopy of halide perovskite materials and devices. *Joule* **2019**, *3*, 641–661.
[157] Timoshenko, J.; Roldan Cuenya, B. *In situ*/operando electrocatalyst characterization by X-ray absorption spectroscopy. *Chem. Rev.* **2021**, *121*, 882–961.
[158] Weidman, M. C.; Smilgies, D. M.; Tisdale, W. A. Kinetics of the self-assembly of nanocrystal superlattices measured by real-time *in situ* X-ray scattering. *Nat. Mater.* **2016**, *15*, 775–781.
[159] Li, T.; Senesi, A. J.; Lee, B. Small angle X-ray scattering for nanoparticle research. *Chem. Rev.* **2016**, *116*, 11128–11180.
[160] Akbali, B.; Topcu, G.; Guner, T.; Ozcan, M.; Demir, M. M.; Sahin, H. $CsPbBr_3$ perovskites: Theoretical and experimental investigation on water-assisted transition from nanowire formation to degradation. *Phys. Rev. Mater.* **2018**, *2*, 034601.
[161] Hills-Kimball, K.; Yang, H. J.; Cai, T.; Wang, J. Y.; Chen, O. Recent advances in ligand design and engineering in lead halide perovskite nanocrystals. *Adv. Sci.* **2021**, *8*, 2100214.
[162] Schmidt, J.; Merkle, A.; Brendel, R.; Hoex, B.; van de Sanden, M. C. M.; Kessels, W. M. M. Surface passivation of high-efficiency silicon solar cells by atomic-layer-deposited $Al_2O_3$. *Prog. Photovolt.: Res. Appl.* **2008**, *16*, 461–466.
[163] Morad, V.; Stelmakh, A.; Svyrydenko, M.; Feld, L. G.; Boehme, S. C.; Aebli, M.; Affolter, J.; Kaul, C. J.; Schrenker, N. J.; Bals, S. et al. Designer phospholipid capping ligands for soft metal halide nanocrystals. *Nature* **2024**, *626*, 542–548.
[164] Kovalenko, M. V.; Scheele, M.; Talapin, D. V. Colloidal nanocrystals with molecular metal chalcogenide surface ligands. *Science* **2009**, *324*, 1417–1420.
[165] Kango, S.; Kalia, S.; Celli, A.; Njuguna, J.; Habibi, Y.; Kumar, R. Surface modification of inorganic nanoparticles for development of organic-inorganic nanocomposites—A review. *Prog. Polym. Sci.* **2013**, *38*, 1232–1261.
[166] López-Fernández, I.; Valli, D.; Wang, C. Y.; Samanta, S.; Okamoto, T.; Huang, Y. T.; Sun, K.; Liu, Y.; Chirvony, V. S.; Patra, A. et al. Lead-free halide perovskite materials and optoelectronic devices: Progress and prospective. *Adv. Funct. Mater.* **2024**, *34*, 2307896.

[167] Xiao, Z. W.; Song, Z. N.; Yan, Y. F. From lead halide perovskites to lead-free metal halide perovskites and perovskite derivatives. *Adv. Mater.* **2019**, *31*, 1803792.
[168] Cai, T.; Dube, L.; Saghy, P.; Yang, H. J.; Chen, O. Progress in all-inorganic heterometallic halide layered double perovskites. *Trends Chem.* **2023**, *5*, 29–44.
[169] Cai, T.; Shi, W. W.; Hwang, S.; Kobbekaduwa, K.; Nagaoka, Y.; Yang, H. J.; Hills-Kimball, K.; Zhu, H.; Wang, J. Y.; Wang, Z. G. et al. Lead-free $Cs_4CuSb_2Cl_{12}$ layered double perovskite nanocrystals. *J. Am. Chem. Soc.* **2020**, *142*, 11927–11936.
[170] Liu, S. P.; Yang, B.; Chen, J. S.; Wei, D. H.; Zheng, D. Y.; Kong, Q. K.; Deng, W. Q.; Han, K. L. Efficient thermally activated delayed fluorescence from all-inorganic cesium zirconium halide perovskite nanocrystals. *Angew. Chem.* **2020**, *132*, 22109–22113.
[171] Han, P. G.; Luo, C.; Yang, S. Q.; Yang, Y.; Deng, W. Q.; Han, K. L. All-inorganic lead-free 0D perovskites by a doping strategy to achieve a PLQY boost from < 2% to 90%. *Angew. Chem.* **2020**, *132*, 12809–12813.
[172] Shi, W. W.; Cai, T.; Wang, Z. G.; Chen, O. The effects of monovalent metal cations on the crystal and electronic structures of $Cs_2MBiCl_6$ (M = Ag, Cu, Na, K, Rb, and Cs) perovskites. *J. Chem. Phys.* **2020**, *153*, 141101.
[173] Saghy, P.; Brown, A. M.; Chu, C.; Dube, L. C.; Zheng, W. W.; Robinson, J. R.; Chen, O. Lanthanide double perovskite nanocrystals with emissions covering the UV-C to NIR spectral range. *Adv. Opt. Mater.* **2023**, *11*, 2300277.
[174] Jellicoe, T. C.; Richter, J. M.; Glass, H. F. J.; Tabachnyk, M.; Brady, R.; Dutton, S. E.; Rao, A.; Friend, R. H.; Credgington, D.; Greenham, N. C. et al. Synthesis and optical properties of lead-free cesium tin halide perovskite nanocrystals. *J. Am. Chem. Soc.* **2016**, *138*, 2941–2944.
[175] Sun, L. H.; Dong, B.; Sun, J.; Wang, Y. M.; Wang, Y. Q.; Hu, S. T.; Zhou, B. S.; Bai, X.; Xu, L.; Zhou, D. L. et al. Efficient and stable multicolor emissions of the coumarin-modified $Cs_3LnCl_6$ lead-free perovskite nanocrystals and LED application. *Adv. Mater.* **2024**, *36*, 2310065.
[176] Yang, B.; Chen, J. S.; Hong, F.; Mao, X.; Zheng, K. B.; Yang, S. Q.; Li, Y. J.; Pullerits, T.; Deng, W. Q.; Han, K. L. Lead-free, air-stable all-inorganic cesium bismuth halide perovskite nanocrystals. *Angew. Chem., Int. Ed.* **2017**, *56*, 12471–12475.
[177] Hao, L. N.; Liu, K.; Cheng, S.; Wang, Y.; Xu, Y. J.; Qian, H. S. $KMnF_3$ nanowires and nanoparticles: Selected synthesis, characterization and magnetic properties. *Mater. Lett.* **2017**, *196*, 145–148.
[178] Gao, Z.; Zhou, H.; Dong, K. L.; Wang, C.; Wei, J. Y.; Li, Z.; Li, J. S.; Liu, Y. J.; Zhao, J.; Fang, G. J. Defect passivation on lead-free $CsSnI_3$ perovskite nanowires enables high-performance photodetectors with ultra-high stability. *Nano-Micro Lett.* **2022**, *14*, 215.
[179] Guo, C. F.; Ren, Z. F. Flexible transparent conductors based on metal nanowire networks. *Mater. Today* **2015**, *18*, 143–154.
[180] Wang, S. L.; Shan, Z. W.; Huang, H. The mechanical properties of nanowires. *Adv. Sci.* **2017**, *4*, 1600332.
[181] Park, H. S.; Cai, W.; Espinosa, H. D.; Huang, H. C. Mechanics of crystalline nanowires. *MRS Bull.* **2009**, *34*, 178–183.
[182] Foster, M. A.; Turner, A. C.; Lipson, M.; Gaeta, A. L. Nonlinear optics in photonic nanowires. *Opt. Express* **2008**, *16*, 1300–1320.
[183] Liu, J. W.; Xu, J.; Liang, H. W.; Wang, K.; Yu, S. H. Macroscale ordered ultrathin telluride nanowire films, and tellurium/telluride hetero-nanowire films. *Angew. Chem., Int. Ed.* **2012**, *51*, 7420–7425.
[184] Li, S. Q.; Lv, C. J.; Luo, H. Y.; Cui, L. H.; Jia, Z. X.; Li, J. F.; Qin, W. P.; Qin, G. S. Ultrathin gold nanowires as broadband saturable absorbers for ultrashort pulsed lasers. *Laser Phys. Lett.* **2022**, *19*, 095102.
[185] Jacobsohn, M.; Banin, U. Size dependence of second harmonic generation in CdSe nanocrystal quantum dots. *J. Phys. Chem. B* **2000**, *104*, 1–5.
[186] Evans, T. J. S.; Schlaus, A.; Fu, Y. P.; Zhong, X. J.; Atallah, T. L.; Spencer, M. S.; Brus, L. E.; Jin, S.; Zhu, X. Y. Continuous-wave lasing in cesium lead bromide perovskite nanowires. *Adv. Opt. Mater.* **2018**, *6*, 1700982.
[187] Kong, Q.; Lee, W.; Lai, M. L.; Bischak, C. G.; Gao, G. P.; Wong, A. B.; Lei, T.; Yu, Y.; Wang, L. W.; Ginsberg, N. S. et al. Phase-transition-induced p-n junction in single halide perovskite nanowire. *Proc. Natl. Acad. Sci. USA* **2018**, *115*, 8889–8894.
[188] Fu, Y. P.; Zhu, H. M.; Stoumpos, C. C.; Ding, Q.; Wang, J.; Kanatzidis, M. G.; Zhu, X. Y.; Jin, S. Broad wavelength tunable robust lasing from single-crystal nanowires of cesium lead halide perovskites ($CsPbX_3$, X = Cl, Br, I). *ACS Nano* **2016**, *10*, 7963–7972.
[189] Wang, J.; Chen, H.; Zhao, Y.; Zhong, Z. B.; Tang, Y.; Liu, G. Z.; Feng, X.; Xu, F. C.; Chen, X. H.; Cai, D. J. et al. Programmed ultrafast scan welding of Cu nanowire networks with a pulsed ultraviolet laser beam for transparent conductive electrodes and flexible circuits. *ACS Appl. Mater. Interfaces* **2020**, *12*, 35211–35221.
[190] Zhao, J.; Lin, R. K.; Wang, J. Y.; Sun, J. Q.; Dong, K. Q.; Zou, H. Y.; Lu, J. Y.; Ma, J. T.; Lu, S. D.; Ma, F. Y. et al. Ultra-thin size-controllable surface plasmon polariton laser by PDMS-assisted imprinting. *J. Phys. D: Appl. Phys.* **2024**, *57*, 405102.